

Army Research Laboratory



Verification of the Aerosol Emissivity Model, PILOT-EX

**By
Robert A. Sutherland**

**Survivability/Lethality Analysis Directorate
Information & Electronic Protection Division**

ARL-TR-2689

July 2002

DEFENSE TECH INFO CENTER
DTIC OCA
8725 JOHN J KINGMAN RD STE 0944
FT BELVOIR VA 22060-6218

Approved for public release; distribution unlimited.

20020729 060

NOTICES

Disclaimers

The findings in this report are not to be construed as an official Department of the Army position, unless so designated by other authorized documents.

Citation of manufacturers' or trade names does not constitute an official endorsement or approval of the use thereof.

DESTRUCTION NOTICE—When this document is no longer needed, destroy it by any method that will prevent disclosure of its contents or reconstruction of the document.

Abstract

We report on the verification of the multiple scattering and thermal emission model PILOT-EX described in a previous publication and extend the scope to include non-isothermal clouds. We also verify the expressions leading to the thermal version of the radiative transfer equation, fill in the details of the Gaussian spherical cloud formulation, describe methods for treating the emissivity correction for limited bandpass instruments, and discuss the significance of the results in terms of radiation contrast and aerosol-induced noise. We extend the model to include arbitrary "embedded sources" and verify results against standards in the literature over a variety of incident angles and demonstrate the significance of the results in computing infrared contrast for use in imaging systems performance analysis. A major finding is that comparisons with known (isothermal) solutions show agreement to within five significant figures for the case of plane layers for both normal incidence and various slant path angles. Also, preliminary results for the case of temperature stratification demonstrate a significant build up of radiance in the (hotter) cloud interior, which leads to lower values of the apparent emissivity for non-isothermal clouds.

Acknowledgements

The original impetus for this work came, in part, from long-range recommendations set forth by the members of the Survivability/Lethality Analysis Directorate Pilot Project originated in 1996. Committee members to be acknowledged are Paul Tannenbaum, Anthony van de Wal, Donald Hemingway, Daniel Hunt, and Lon Anderson. Others who helped with testing early versions of the model(s) include Lee Butler, Jon Anderson, Andre Bevic, James Nealon, and Scarlett Ayres.

Preface

The main purpose of this report is to serve as a follow up to a previous report describing the main features and utility of the PILOT-EX model used to generate exact solutions of the thermal and optical versions of the radiative transfer equation. There are roughly seven topics covered, some of which are ancillary to our previous report and others that can be treated as “stand alone” but are nevertheless related to the previous work.

Table of Contents

Abstract	i
Acknowledgements	ii
Preface	iii
Executive Summary	vii
1. Introduction	1
2. Thermal Version of the Radiative Transfer Equation	1
3. Gaussian Cloud Formulation	6
4. Radiance Distribution in Gaussian Clouds	11
5. Verification of Pilot-Ex (Isothermal Plane Layers)	14
6. Bandpass Functions and Apparent Temperature	20
7. Radiation Contrast (Thermal Derivative)	25
8. Effect of Aerosol-Induced Noise	27
9. Temperature Stratification	30
10. Summary	32
References	33
SF 298	34

Figures

1. Sketch demonstrating the differential radiative transfer equation	8
2. Sketch of Gaussian cloud formulation and nomenclature	12
3. Example of optical and spatial representation for Gaussian cloud	16
4. Two dimensional arrays of transmissivity, emissivity and reflectivity	18
5. Cross-sectional plots of transmissivity, emissivity and reflectivity.....	19
6. Sketch demonstration Plane Layer nomenclature.....	20
7. Source functions for plane layers: (a) reflection, (b) emission.....	21
8. Relative intensity functions for plane layers: (a) reflectivity, (b) emission.....	24
9. Bandpass functions: radiance, left; thermal derivative, right	27
10. Spectral plots to demonstrate concept of apparent temperature	28
11. Emissive source functions for non-isothermal clouds	37

Tables

1. Comparison of calculated reflectivities for normal incidence with plane layers.....	22
2. Comparison of calculated reflectivities and emissivities for various slant angles.....	25
3. Hypothetical data for bandpass example	27

Executive Summary

This report is the second in a series of reports documenting the development and verification of the U.S. Army Research Laboratory PILOT-EX aerosol emissive effects model. An earlier report covered the general concepts, a short theoretical development, and some preliminary verification with limiting cases. In this we report we fill in many of the mathematical details of the model, provide many more cases for verification, and extend the scope to include non-isothermal clouds. We also verify the expressions leading to the thermal version of the radiative transfer equation, fill in the details of the Gaussian cloud formulation, describe methods for treating the emissivity correction for limited bandpass instruments, and discuss the significance of the results in terms of radiation contrast and aerosol-induced noise, which we relate to the problem of computing infrared contrast, familiar to the user community and used in imaging systems performance analysis. On the theoretical development, we also extend the model to include arbitrary "embedded" radiation sources and verify results against standards in the literature over a variety of incident angles. This development could be of significance to modeling (hot) missile plume signatures. A major theoretical finding is that comparisons with known (isothermal) solutions show agreement to within five significant figures for the case of plane layers for both normal incidence and various slant path angles. Also, preliminary results for the case of temperature stratification demonstrate a significant build up of radiance in the (hotter) cloud interior, which leads to lower values of the apparent emissivity for non-isothermal clouds. The details given here along with those also given in our initial report offer a complete solution to the radiative transfer equation for finite aerosol clouds of radial symmetry. The method addresses both aerosol thermal emission as well as reflection, including all orders of multiple scattering. The method represents exact solutions that compare favorably with other studies when applied to plane layers. We have also demonstrated the significance of the results in systems evaluation through the effect on the thermal derivative, or "radiation contrast," used in evaluating infrared scanning systems such as the FLIR (forward-looking infrared). The methodology, *per se*, is applicable only to isothermal clouds and isotropic scattering although these are not necessarily fundamental limitations on the method. In yet another study we have extended the method to include non-isothermal clouds, non-isotropic scattering, and other practical effects using various approximations.

1. Introduction

The main purpose of this report is to serve as a follow up to a previous report, which described the main features and utility of the PILOT-EX model used to generate exact solutions of the thermal and optical versions of the radiative transfer equation [1]. There are roughly seven topics covered, some of which are ancillary to our previous report and others that can be treated as "stand alone" but are nevertheless related to the previous work. Sections 2, 4 and 5 are examples of the former type which cover such details as; the formulation of the radiative transfer equation to include natural thermal emission in section 2, the details of the Gaussian cloud formulation borrowed from the COMBIC [2] model in section 3, and the verification of the model by comparisons with other methods from the literature in section 5. In section 4 we give an example of some interesting manifestations of the exact solutions which, when applied to Gaussian clouds, give rise to various effects such as infrared "edge brightening," which is often associated with visible wavelengths and natural clouds. We extend the scope of the study somewhat in sections 6, 7, and 8, by addressing such issues as sensor bandpass effects and the definition of apparent temperature in an obscuring environment (section 6), the concept of radiation contrast for small differential signal analysis (section 7), and the effect of aerosol-induced path radiance on system performance parameters such as the signal-to-noise ratio (section 8). In section 9 we extend the formulation to include thermal stratification and define a practical, or "effective," emissivity to augment the previous work which treated the isothermal case only.

2. Thermal Version of the Radiative Transfer Equation

Although the thermal emission term discussed in section 3 of our previous paper [1] seems clear and intuitive, there are some fundamental difficulties in justifying the form when used in realistic atmospheric applications. The root of the difficulty lies in the use of the Blackbody function, $B(\lambda, T)$, which requires that the system, atmosphere, and aerosol cloud be in strict thermodynamic equilibrium, a condition certainly not valid for any realistic scenario that we wish to address. To solve the non-equilibrium problem rigorously would require an in-depth look at the kinetics of thermal motion and going far beyond the relatively simple Maxwell-Boltzman treatment in the classical texts and certainly beyond the scope of the treatment here. Fortunately, there is a practical alternative using the concept of "local thermodynamic equilibrium" which has been rigorously established as valid for most atmospheric applications and which we will apply here [3].

We begin with the differential version of the "standard" radiative transfer equation [4,5] for computing the total radiance, $I(r)$, including both the directly transmitted component and any contributions to multiple in-scattering as (fig. 1):

$$\frac{1}{C(r)} \frac{dI(r)}{dr} = -(k_{\text{abs}} + \sigma_{\text{sct}})I(r) + \sigma_{\text{sct}} J_{\text{src}}(r) \quad (1)$$

where $C(r)$ is the aerosol mass concentration and (k_{abs}, σ_{sct}) are, respectively, the mass absorption and mass scattering coefficients which, in turn, are related to the more usual mass extinction coefficient and single scattering albedo as

$$\alpha = k_{abs} + \sigma_{sct} \quad (2a)$$

$$\omega_o = \frac{\sigma_{sct}}{k_{abs} + \sigma_{sca}} \quad (2b)$$

which are the same definitions used in our previous paper, although we have altered the notation slightly to conform with cited references. The major unknown in eq. (1) is the so-named (optical) source function, $J_{src}(r)$, which we ultimately seek to determine. The differential, $dI(r)$, in eq. (1) applies to a small cylindrical volume of differential thickness, dr , aligned along the propagation vector, r , as sketched in figure (1).

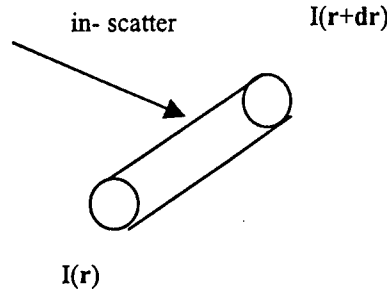


Figure 1. Sketch demonstrating the differential radiative transfer equation.

In eq. (1), the first term on the right accounts for losses due to both absorption and out-scatter (i.e., extinction) along the main beam and the second accounts for in-scatter of ambient radiative sources (sky and surface) from all directions. Without committing to any specific mathematical form, we next add an *ad hoc* emission term to the right side of eq. (1) as follows:

$$\frac{1}{C(r)} \frac{dI(r)}{dr} = -(k_{abs} + \sigma_{sct})I(r) + \sigma_{sct} J_{src}(r) + \frac{1}{C(r)} \frac{dI_{ems}}{dr} \quad (3)$$

where the added term, at this point, could include any type internal, or “embedded,” radiation source, either artificial or natural. For the special case treating thermal emission, it is plausible to seek an expression defining an aerosol mass emission coefficient analogous to the mass absorption and mass scattering coefficients such that

$$\frac{1}{C(r)} \frac{dI_{ems}}{dr} = e_{ems} B(\lambda, T) \quad (4)$$

where $B(\lambda, T)$ is the Planck Blackbody function, λ is the wavelength, and T is the real (i.e., thermodynamic) temperature of the aerosol and can be a function of r if we include thermal stratification as we will do in section 8. In eq. (4) we have introduced e_{ems} , as an *ad hoc* “mass

emission coefficient" analogous to the mass absorption and mass scattering coefficients, k_{abs} and σ_{sct} . To specifically address the case of natural thermal emission, we next introduce the equilibrium version of the radiative transfer equation as follows:

$$\frac{1}{C(r)} \frac{dI}{dr} = -k_{\text{abs}} B(\lambda, T) + \frac{1}{C(r)} \frac{dI_{\text{ems}}}{dr} \quad (5)$$

from which we can immediately reproduce a version of Kirchoff's relationship by invoking the equilibrium condition as $[dI/dr=0]$ to yield

$$\frac{1}{C(r)} \frac{dI_{\text{ems}}}{dr} = k_{\text{abs}} B(\lambda, T) \quad (6)$$

which, from comparison with eq. (4), immediately requires the mass emission coefficient to be equal to the mass absorption coefficient (i.e., $e_{\text{ems}}=k_{\text{abs}}$), which is the essence of Kirchoff's Law as applied to an aerosol medium.

We now formally apply the concept of local thermal equilibrium to the problem at hand by inserting eq. (6) into eq. (3) to yield the following:

$$\frac{1}{C(r)} \frac{dI(r)}{dr} = -(k_{\text{abs}} + \sigma_{\text{sct}})I(r) + \sigma_{\text{sct}} J'_{\text{src}}(r) + k_{\text{abs}} B(\lambda, T) \quad (7)$$

which, at this point, we cautiously refer to as an approximation and make explicit the fact that the (new) source function, J'_{src} , must now include not only the effect of multiple in-scatter from external sources (as before), but also must include the multiple scattering contribution of the internal thermal emissions which come from all parts of the cloud. Next we rewrite eq. (7) to explicitly account for both an ambient (external in-scatter) part and an emissive (internal scattering) part as

$$\frac{1}{C(r)} \frac{dI(r)}{dr} = -(k_{\text{abs}} + \sigma_{\text{sct}})I(r) + \sigma_{\text{sct}} J_{\text{ext}}(r) + \sigma_{\text{sct}} J_{\text{int}}(r) + k_{\text{abs}} B(\lambda, T) \quad (8)$$

which is consistent with the concept defining the total source function as the sum of the ambient and emissive components [i.e., $J'_{\text{src}}(r) = J_{\text{ext}}(r) + J_{\text{int}}(r)$] as was done our earlier work.

The degree to which the approximation implicit in eq. (8) holds depends upon the degree to which the atmosphere/aerosol system is in local thermodynamic equilibrium. For the atmosphere in general, many studies have shown the approximation to be valid up to an altitude of about 50,000 km, above which the Maxwell-Boltzman distribution is not necessarily maintained and, thus, strict equilibrium as applied here becomes invalid. The inclusion of aerosol particles does not present a big conceptual problem because it is the surrounding and intervening air molecules that actually provide the thermal agitation required to maintain thermal equilibrium. However, there is a need to assure good thermal mixing so that the temperature of the aerosol particles and

the surrounding air molecules remain in near thermal equilibrium, which is a valid assumption here if we assume the aerosol particles to be small. There may be other applications wherein the accuracy of the above derivation may come into question; however, the final expressions as given here have been more or less been accepted as valid approximations for most engineering applications [6].

Owing to the linearity of the underlying expressions, it is clear from both a mathematical and physical sense that the problem can be solved in two parts by separating the external and internal contributions. That is, we can rewrite eq. (8) in the form of two differential equations that we will refer to as the “optical” and “thermal” versions of the radiative transfer equation. That is,

optical version :

$$\frac{dI(\tau)}{d\tau} = -I(\tau) + \omega_o J_{\text{ext}}(\tau) \quad (9a)$$

thermal version :

$$\frac{dI(\tau)}{d\tau} = (1 - \omega_o) B_{\Delta\lambda}^*(\tau; T) + \omega_o J_{\text{int}}(\tau) \quad (9b)$$

where we have also made two major substitutions; the first by using eq. (2) to insert the mass extinction coefficient [$\alpha = k_{\text{abs}} + \sigma_{\text{sca}}$] and albedo [$\omega_o = \sigma_{\text{sca}} / (k_{\text{abs}} + \sigma_{\text{sca}})$], and the second to replace the spatial variable, r , with the path optical thickness, τ [$\tau = \tau(r, r_o)$]. Following conventional practice, we now define the optical thickness between any two points in terms of the concentration path integral as [note $d\tau = \alpha C(r) dr$]:

$$\tau(r_o, r) = \int_{r_o}^r d\tau' = \int_{r_o}^r \alpha C(r') dr' \quad (10)$$

where it is understood that the integration proceeds along the straight line path connecting the two points r_o and r .

For the special case, $J_{\text{ext}} = J_{\text{int}} = 0$, both expressions in eq. (9) can be integrated immediately to yield the following “zeroth” order, or Beer’s Law, solutions; that is,

optical version :

$$I_{\text{dir}}(\tau) = I(r_o) e^{-\tau(r, r_o)} \quad (11a)$$

thermal version :

$$J_{\text{dir}}(\tau) = (1 - \omega_o) \int_0^{\tau} B_{\Delta\lambda}^*(\tau', T) e^{-\tau'(r', r_o)} d\tau' \quad (11b)$$

which are identical in form to what we termed the direct contributions discussed in [1].

The differential expressions of eq. 9 can be converted to integral expressions by formally integrating both sides of the equations. Following the usual procedure, we first multiply each side by an integrating factor of the form $e^{+\tau}$ and then integrate along an arbitrary path whereupon we have, from eq. (9a), after some slight rearrangement,

$$\int_0^\tau \left[\frac{dI(\tau')}{d\tau'} e^{+\tau'} + I(\tau') e^{\tau'} \right] d\tau' = \omega_0 \int_0^\tau J_{src}(\tau') e^{\tau'} d\tau' \quad (12a)$$

or

$$\int_0^\tau \frac{d[I(\tau') e^{\tau'}]}{d\tau'} d\tau' = \omega_0 \int_0^\tau J_{src}(\tau') e^{\tau'} d\tau' \quad (12b)$$

where, in the second expression, the term on the left side follows directly from the chain rule for differentiation and can be integrated immediately to yield

optical version :

$$I(\tau) = I_0 e^{-\tau} + \omega_0 \int_0^\tau J_{ext}(\tau') e^{-(\tau-\tau')} d\tau' \quad (13a)$$

where we have performed the (trivial) integration on the left side of eq. (12b) and divided through by the integrating factor, e^τ . Written as such, eq. (13a) is the integral form equivalent of eq. (9a). The treatment for the thermal version proceeds in the same manner and ultimately leads to

thermal version :

$$I(\tau) = (1 - \omega_0) \int_0^\tau B(\lambda, T) e^{-(\tau-\tau')} d\tau' + \omega_0 \int_0^\tau J_{int}(\tau') e^{-(\tau-\tau')} d\tau' \quad (13b)$$

which accounts for all radiance emanating from the aerosol cloud and does not include the direct contribution from the target which has already been accounted for in the "optical" version. We can think of the first term on the right side of eq. (13b) as a direct (emissive) component accounting for all direct (aerosol) emissions along the path, very much analogous to the (hard target) direct term of eq. (13a). Equations (13a) and (13b) are valid for any geometric shape and form the basis for the multiple scattering solutions throughout our previous work in [1].

Although we have focused here on (natural) thermal emission, it turns out that the derivation can also be applied to the more general case treating any (artificial) embedded source of arbitrary form. The derivation is similar to that described above except that we need not necessarily be concerned about the condition of thermal equilibrium. Thus we recast eq. (4) in a more general form as

$$\frac{1}{C(r)} \frac{dI_{emb}}{dr} = j_{emb}(r) \quad (14)$$

where j_{emb} is referred to as the “emission coefficient” and may or may not be a function of the cloud temperature. In eq. (14) we have used the subscript “emb” to stand for “embedded” sources following the general ideas of the classical texts. We can now retrace the steps leading to eq. (13) and introduce one more expression to address the general emissive case as

embedded sources :

$$I(\tau) = \int_0^{\tau} j_{\text{emb}}(\tau') e^{-(\tau-\tau')} d\tau' + \omega_0 \int_0^{\tau} J_{\text{emb}}(\tau') e^{-(\tau-\tau')} d\tau' \quad (15)$$

where $j_{\text{emb}}(\tau)$ is some, as yet unspecified, function serving the same purpose as the direct emissive component in the thermal case and $J_{\text{emb}}(\tau)$ is the multiple scattering contribution. In section 4 we will test eq. (15) and compare with the classic results of Van de Hulst [5].

3. Gaussian Cloud Formulation

In this section we develop the “standard” Gaussian cloud formulation used in the source function calculations. The main objective is to develop the analytical expressions needed for calculating the optical thickness, $\tau(\mathbf{r}, \mathbf{r}_0)$, between any two points, \mathbf{r} and \mathbf{r}_0 , assuming a Gaussian aerosol cloud centered at the origin as sketched in figure 2. With reference to figure 2, the task is to calculate the optical thickness along the dashed path beginning at some arbitrary point \mathbf{r} and proceeding outward to the practical “edge” of the cloud indicated by the dashed arc at \mathbf{r}_0 , which corresponds to \mathbf{R}_0 , the cloud “practical” radius.

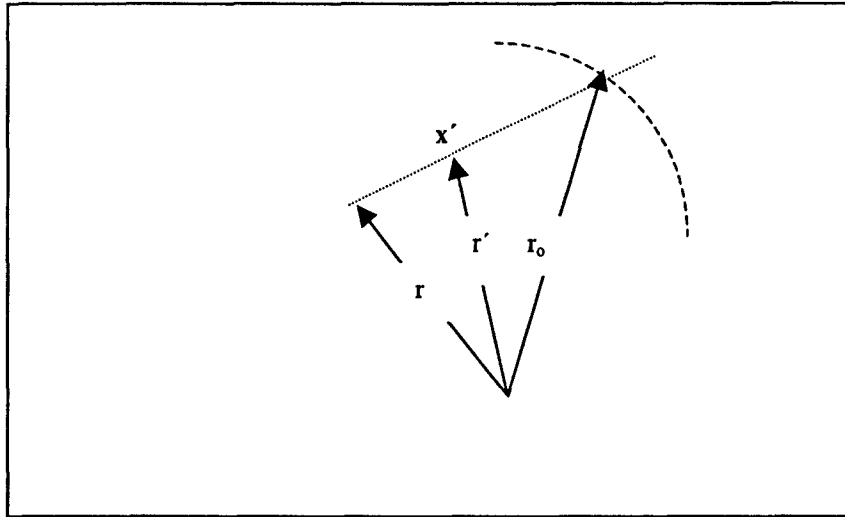


Figure 2. Sketch of Gaussian cloud formulation and nomenclature.

For a constant mass extinction coefficient, α , it follows from the definition of eq. (10) in the previous section that the major computational burden lies in computing the path integrated

concentration, or "CL Product," which, for the case of a Gaussian concentration distribution, is written as

$$CL(r, r_o) = \int_r^{r_o} C(r') dr' = \frac{Q_o}{(\sqrt{2\pi}\sigma_o)^3} \int_r^{r_o} \exp\left[-\frac{r'^2}{2\sigma_o^2}\right] dr' \quad (16)$$

where, as noted in figure 2, the point indicated by the vector, r' also corresponds to a vector distance x' from the integration starting point.

From simple vector geometry and figure 2 we have $[r' = r + x']$, which we next substitute into eq. (16) to yield

$$CL(r, r_o) = \frac{Q_o}{(\sqrt{2\pi}\sigma_o)^3} \int_0^{x_o} \exp\left[-\frac{(r+x')^2}{2\sigma_o^2}\right] dx' \quad (17)$$

where we have also made explicit the fact that the integration proceeds along the straight line path, x' , starting at $x'=0$ and ending at $x'=x_o$, as indicated in the sketch of figure 2. In eq. (17), the parameters Q_o and σ_o are known constants representing, respectively, the cloud total mass (grams) and the Gaussian half width (meters) and are determined in a manner described later in this section.

The next objective is to express eq. (17) into a more workable scalar form. We do this by first expanding the exponential argument in the above expressions by applying simple vector geometry to obtain the following:

$$\begin{aligned} r'^2 &= [r + x']^2 \\ &= |r|^2 + |x'|^2 + 2rx'(\hat{r} \cdot \hat{x}') \\ &= x'^2 + r^2 + 2rx'\mu \\ &= (x' + \mu r)^2 + r^2(1 - \mu^2) \end{aligned} \quad (18)$$

where μ is the cosine of the angle between the radial vector, r , and the propagation vector, x' (or x_o , since the two are collinear). The form of the last expression in eq. (18) follows from simple geometry with some minor manipulation and can be verified by direct expansion.

We now rewrite eq. (17) with the aid of eq. (18) into a more workable (scalar) form for subsequent integration as follows:

$$\begin{aligned}
CL(r, r_o; \mu) &= \frac{Q_o}{(\sqrt{2\pi}\sigma_o)^3} \int_0^{x_o} \exp\left[-\frac{(x'+\mu r)^2 + r^2(1-\mu^2)}{2\sigma_o^2}\right] dx' \\
&= \frac{Q_o}{(\sqrt{2\pi}\sigma_o)^3} \exp\left(-\frac{r^2(1-\mu^2)}{2\sigma_o^2}\right) \int_0^{x_o} \exp\left[-\left(\frac{x'+\mu r}{\sqrt{2}\sigma_o}\right)^2\right] dx' \\
&= C_1 \int_0^{x_o} \exp\left[-\left(\frac{x'+\mu r}{\sqrt{2}\sigma_o}\right)^2\right] dx' \tag{19}
\end{aligned}$$

where we have made explicit the fact that the expression as now written is dependent upon the scalar variables (r, r_o, μ) . The constant, C_1 , turns out to be numerically equal to aerosol mass concentration at the integration starting point [i.e., $C_1 = C(r)$] and can be calculated accordingly. It is of some importance to note from the form of eq. (19) that the final integrated result is dependent only upon the relative angle, μ , and the scalar distances (r, x_o) where x_o is the total path distance [$x_o^2 = r^2 + r_o^2$]. This fact was found to be important in applying the mathematics for evaluating the source function in [1].

Following the usual approach we next introduce the intermediate variable, $t'^2 = (x' + \mu r)^2 / 2\sigma_o^2$, allowing us to compress eq. (19) into the following form:

$$CL(r, r_o; \mu) = \sqrt{2}\sigma_o C_1 \int_0^{t_o} \exp[-t'^2] dt' \tag{20}$$

where we have also substituted, $dt' = dx' / \sqrt{2}\sigma_o$. The major advantage gained from all this manipulation lies in the fact that the integral in eq. (20) can now be expressed in terms of the well-known error function and can thus be integrated immediately as follows:

$$\begin{aligned}
CL(r, r_o; \mu) &= \sqrt{2}\sigma_o C_1 \left\{ \int_0^{t_o} \exp[-t'^2] dt' - \int_0^t \exp[-t'^2] dt' \right\} \\
&= \sqrt{\pi/2}\sigma_o C_1 \{ \text{erf}(t_o) - \text{erf}(t) \} \\
&= CL_o \left\{ \text{erf}\left(\frac{x_o + \mu r}{\sqrt{2}\sigma_o}\right) - \text{erf}\left(\frac{\mu r}{\sqrt{2}\sigma_o}\right) \right\} \tag{21}
\end{aligned}$$

where CL_o is a another constant ($CL_o = \sqrt{\pi/2}\sigma_o C_1$) which turns out to be numerically equal to the total "center-to-edge," or CL radial path and will be discussed more fully in the following paragraphs.

The error function as used in eq. (21) is defined formally for our applications in the usual notation as

$$\text{erf}(x) = \frac{2}{\sqrt{\pi}} \int_0^x e^{-t'^2} dt' \quad (22)$$

which can be evaluated readily using any of a number of numerical approximations described in the standard handbooks [7].

In actually applying the above formulation to the task at hand, all calculations are performed on a "standard" cloud of fixed radius R_o representing the "practical" extent of the Gaussian cloud (which strictly extends to infinity). For practical purposes we arbitrarily define the edge as the point where the concentration drops to 1/1000 of the value at the centroid. We furthermore define the total mass of this standard cloud such that the total edge-to-edge CL path, or "CL diameter," calculates to unity. After some manipulation, this leads to the following values for the "standard" cloud:

$$\begin{aligned} \sigma_o &= R_o / \sqrt{2 \ln(1000)} = 13.452 \\ Q_o &= 2\pi\sigma^2 / (\text{erf}(R_o / \sqrt{2}\sigma) = 1350.0 \end{aligned} \quad (23)$$

where the numerical values shown correspond to calculations performed using a cloud of one meter diameter [i.e., $R_o = D_o/2 = 0.50(\text{m})$] and are the actual values used throughout the calculations. With the Gaussian parameters so determined, the calculation of the CL Product over any path inside the cloud is readily found from eq.(21) from which the optical thickness is then simply

$$\tau(r, r_o; \mu) = \alpha \text{CL}(r, r_o; \mu) \quad (24)$$

which follows directly from the defining equation, eq. (10), of the previous section.

It is important to note from eq. (24) that we can vary the cloud optical thickness in either of two ways: (1) either by changing the optical variable, α , or (2) by changing the cloud concentration through the Gaussian parameters Q_o or σ_o . It turns out that these two methods are totally equivalent and are part of the basis for the optical thickness (not r) being the "real" independent variable for the optical calculations. This means that once we have done the calculations for our "standard" unit cloud, the results are valid for *any* cloud of the same optical depth, regardless of the spatial extent—a circumstance that makes the formulation much more universal than it might at first appear.

To summarize this section we show a numerical example in figure 3 of some edge-to-edge cross-sectional plots of concentration and CL Product for our standard cloud using the parameters of eq. (23) assuming a unit cloud diameter (i.e., $R_o = D_o/2 = 0.50$).

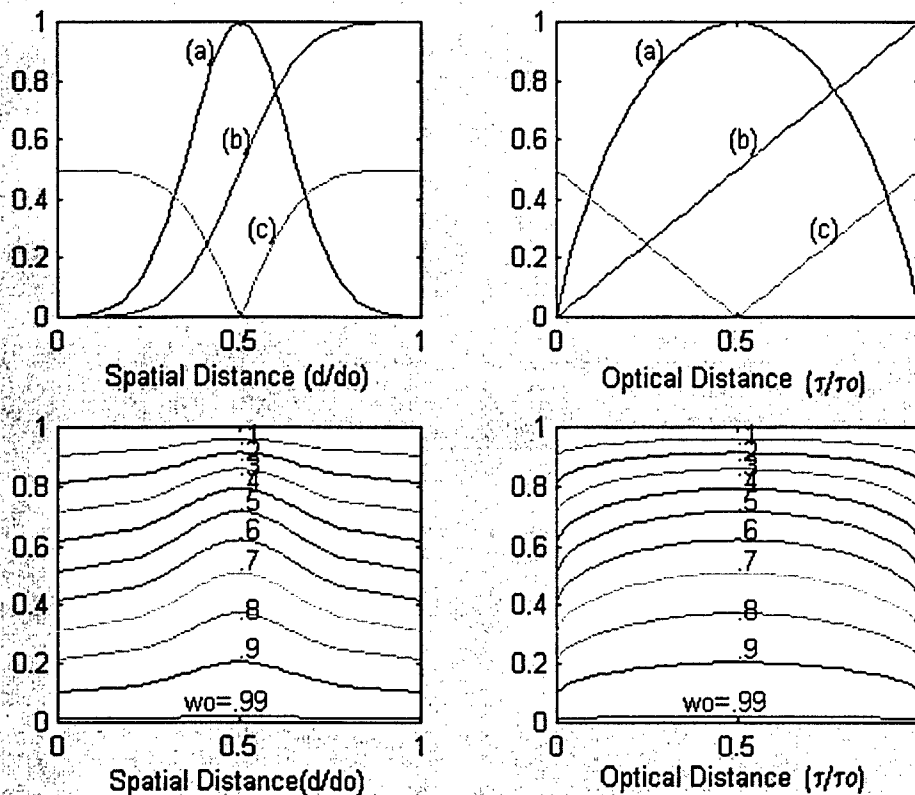


Figure 3. Example of optical and spatial representation for Gaussian cloud.

Referring to the upper two plots of figure 3, those on the left are based upon the usual spatial representation where the abscissa represents linear distance referenced from the (left) edge of the cloud and passing through the cloud centroid. The plots on the right represent the same numerical data, but we use the CL Product as the abscissa instead of the spatial distance. Note that we label the axes as either normalized spatial distance (d/d_0) or normalized optical distance (τ/τ_0). In both cases the curves labeled (a) represent the concentration (normalized to unity at the center), the curves labeled (b) represent the CL Product referenced to zero from the left edge, and the curves labeled (c) represent the "radial" CL Product reference to zero at the midpoint. Note from the plots the obvious radial symmetry with the concentration maximum at the center and the CL Product rising from a value of zero at the left edge to a value of 0.50 at the center and finally to a value of unity at the right edge. The radial CL Product is zero at the center and increases to a maximum value of 0.50 toward either edge. Clearly, in the plots on the right the optical thickness appears as a straight line as it must and the concentration plot is much broader in appearance.

In the lower plots of figure 3, we show another example in how the choice of representation affects the appearance of the source functions described in [1]. The particular examples shown here represent the emissive source function based on a cloud optical thickness, or "optical diameter," of unity (i.e., $\tau_0=1$). The various curves in each plot represent albedo ranging from zero and increasing to unity in the direction shown. Clearly, the main difference between the two representations is that the optical version produces generally broader plots than the spatial

versions and might offer some analytical advantages. Our experience is that the optical representation is more natural and is usually easier to work with analytically.

4. Radiance Distribution in Gaussian Clouds

In our main paper we made mention that the behavior of the reflectivity functions could lead to some interesting effects on cloud images. In particular the fact that the reflectivity functions show a maximum at moderate optical thickness can lead to an edge brightening under certain conditions that is often observed for natural clouds at visible wavelengths. Some insight into how this comes about can be gained by looking more closely at the various relationships existing among the transmissivity, t_{aer} , emissivity, ε_{aer} , and reflectivity, r_{aer} , functions, especially the continuity relationship, which we rewrite here as

$$t_{\text{aer}}(\tau) + \varepsilon_{\text{aer}}(\tau) + r_{\text{aer}}(\tau) = 1 \quad (25)$$

which is valid for any path through an isothermal cloud.

We demonstrate these relationships in the two-dimensional arrays of figure 4 which were generated by applying eq. (30) of our main paper along multiple parallel paths traversing the entirety of a Gaussian cloud. In constructing figure 4, we assumed a 100 by 100 m Gaussian array of 1 m resolution and standard deviation, σ_0 , of 30.0 m. In figure 4 the first three columns refer to transmissivity, emissivity, and reflectivity, respectively, as calculated using the source functions for an isothermal cloud. Each row in figure 4 corresponds to a specific edge-to-edge centerline optical thickness ranging from $\tau=0.50$ (upper row) to $\tau=8.0$ (bottom row) as indicated in the side margins. Out of curiosity we have also included, in the last column, a difference array between the emissivity and reflectivity, which according to the continuity condition, should be of the form $[1-e^{-\tau}]$. In all cases the albedo is set to $\omega_0=0.50$.

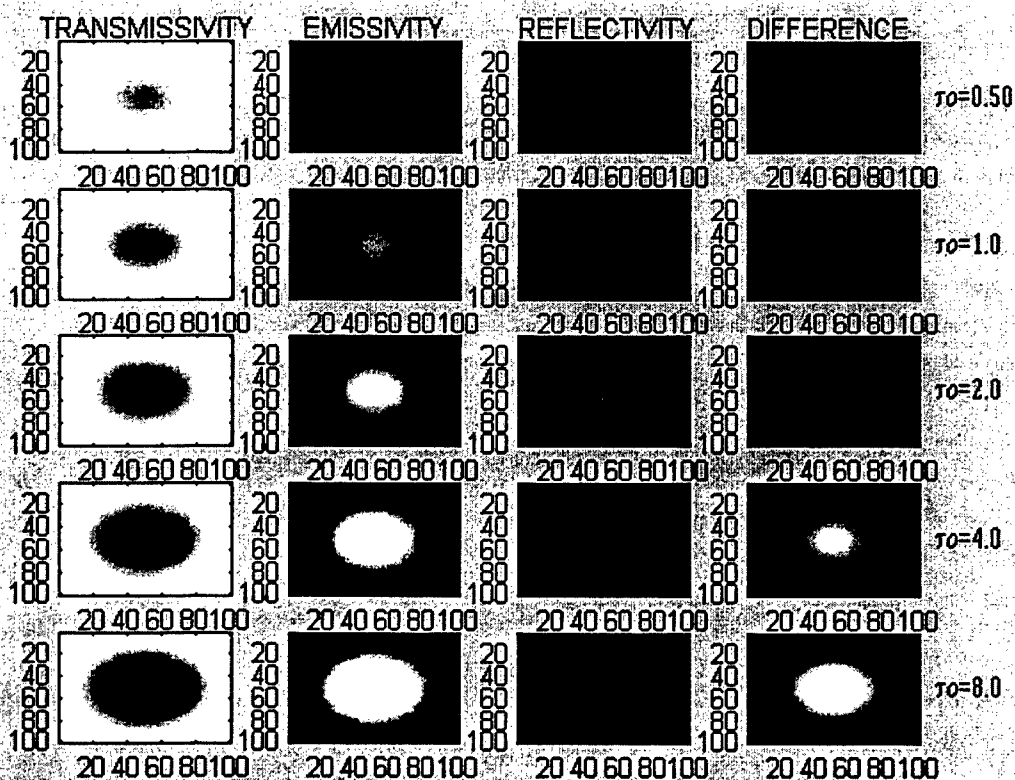


Figure 4. Two dimensional arrays of transmissivity, emissivity and reflectivity.

In analyzing the results of figure 4, the transmissivity (first column) and emissivity (second column) trends are the most easy to interpret in that they show a general monotonic increase in magnitude with increasing optical thickness, which also gives rise to an apparent increase in the perceived “size” of the resultant cloud. The reflectivity (third column) shows a similar increase with increasing optical thickness but not nearly as marked as is the case for emissivity. This difference in cloud “brightness” occurs in spite of the fact that the (single scattering) albedo of 0.50 indicates equal fractions of absorption and scattering at the particle level. The most curious feature in figure 4 is the appearance of a darkened center for the reflective case that becomes more and more pronounced as the optical thickness increases and is perceived as an actual decrease in reflectivity at the center. This “darkening” effect is real and is related to the maximum in reflectivity discussed in our main paper, but is more easily explained as a manifestation of the continuity relationship.

We probe this “brightening” effect more quantitatively in figure 5 where we show side-by-side cross-sectional plots of emissivity and reflectivity for a wide range of situations.

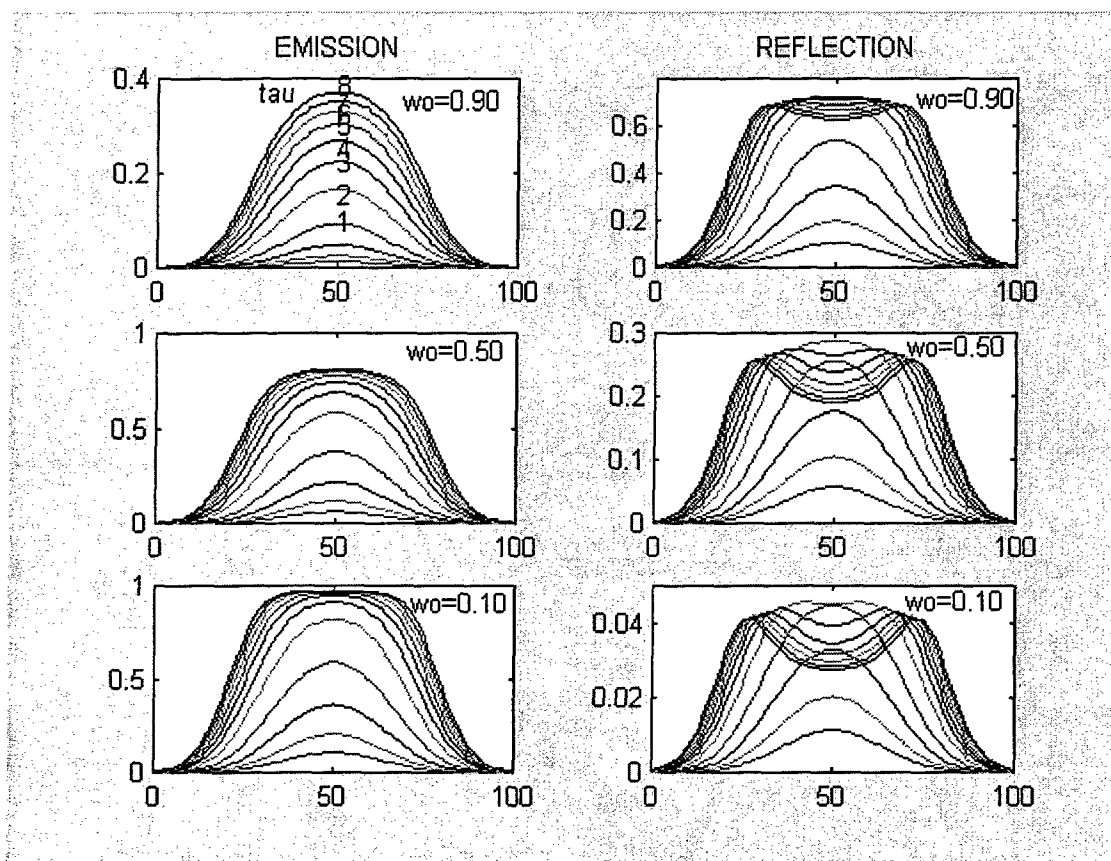


Figure 5. Cross-sectional plots of transmissivity, emissivity, and reflectivity.

The plots in figure 5 show results of calculations for both emissivity (left) and reflectivity (right) for three values of albedo: .90 (top), 0.50 (middle), and 0.10 (bottom). Each subplot includes 11 curves representing optical thicknesses ranging from 0.125 to 10.0 which occur in an increasing monotonic order with the exception for the center values in the reflective case. In figure 5, the general trend for the emissivity curves is toward a monotonic increase in emissivity with increasing optical thickness which holds for all albedos. It is also generally true from the three examples that the effect of an increased albedo is to lower the emissivity (note y-axis scales). There is also a tendency for the emissivity curves to "flatten out" and mesh together as the optical thickness increases, an effect that is more and more pronounced as the albedo decreases, and in the extreme gives rise to a broad maximum in the curves which mesh toward unity at the highest optical thicknesses. The reflectivity curves show a similar behavior except that the effect of albedo is reversed in the sense that an increased albedo gives rise to a higher reflectivity (note y-axis scale changes), and the curves not only tend to "flatten out" but actually decrease in the center as the optical thickness increases beyond a value between about 1 or 2. From figure 5, the effect becomes more and more marked as the albedo decreases. This decrease in the center, also evident in figure 4, is often perceived as an increase at the cloud edges often observed in natural clouds in the sunlit sky and has also been observed in single scattering models at visible wavelengths [8].

5. Verification of Pilot-Ex (Isothermal Plane Layers)

Although the main emphasis here is on finite clouds of spherical symmetry, it turns out that the multiple scattering method described in our earlier paper also applies to plane layer symmetry for which there are other studies to compare results, the most comprehensive being the extensive tables published by van de Hulst [5]. Our purpose in this section is to use the plane layer results as a verification of our method for computing the emissive and reflective source functions. As it happens, there is actually very little data for direct comparisons of the source functions, *per se*; however, there are extensive tables for the integral quantities, like reflection and to a lesser extent emission, which will be main basis for the comparisons. A sketch of the relevant geometry for the plane layer is shown in figure 6.

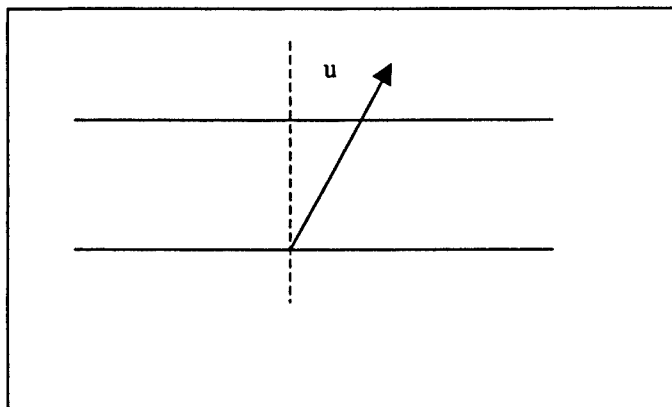


Figure 6. Sketch demonstration Plane Layer nomenclature.

For the plane layer case we need only replace the three-dimensional Gaussian concentration functions with the more easily treated one-dimensional form, which ultimately results in the following simple expression for the slant path optical thickness:

$$\tau(z, \mu) = \frac{\tau_v(z)}{u} \quad (26)$$

where $\tau_v(z)$ [$=\tau(z, 1)$] is the optical depth measured over the vertical spatial distance, z , and u [$u=|\mu|$], is the absolute value of the cosine of the slant path angle (fig. 6). For this study the vertical optical depth is modeled as a Gaussian function with the centroid at the vertical midpoint of the layer and again is based on a "standard" cloud with parameters selected such that the vertical edge-to-edge CL product taken through the entirety of the layer calculates to unity.

It follows directly from inspection of eq. (26) that the condition of azimuthal symmetry holds so that we can apply the methodology of section 3 in our previous report. It also turns out that for

the plane layer case the (numerous) angular integrations can be performed analytically by employing the Exponential Integral,

$$I = \int_{-1}^{+1} e^{-\tau/u} du = E_2(\tau/u) \quad (27)$$

where $E_2(x)$ is the well known second order Exponential Integral which was evaluated using established numerical approximations [7]. Other than Eq. (26) and (27) there were no other substantive changes needed to address the plane layer case.

In figure 7 we show the results of calculations for the plane layer using the same general scheme that was used for the spherical clouds in our earlier work (fig. 5) [1]. The calculations are based upon the normalized source functions and thus vary in overall magnitude from zero to unity. The abscissa, for the plane layer case, is the edge-to-edge, or better, "top-to-bottom" normalized optical thickness referenced along the vertical from top to bottom.

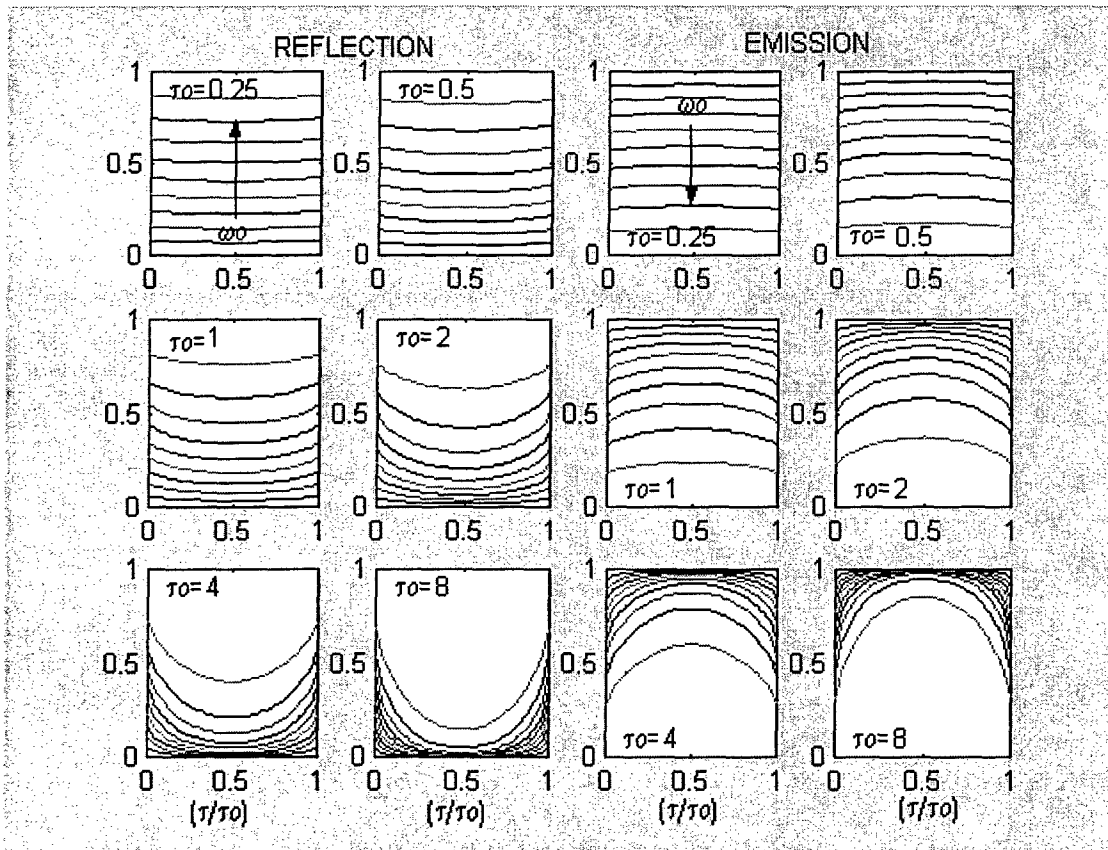


Figure 7. Source functions for plane layers: (a) reflection, (b) emission.

The layout in figure 7 is identical to that of figure 3 and show the reflective case on the left and the emissive case on the right. For each case there are six subplots corresponding to six values of cloud total optical thickness ranging from $\tau_0=0.250$ to 8.0, as indicated on the figures. The various curves in each subplot correspond to albedos ranging from zero to unity in steps of $\Delta\omega=0.10$ and, as before, either increase in overall magnitude with increasing albedo (reflective)

or decrease in overall magnitude with increasing albedo (emissive), as indicated by the direction of the arrow on the uppermost plots. The calculations were performed over a vertical path (i.e., $\mu=1$) so that the comparisons with the spherical results (taken along the cloud centerline) are on a common basis as far as the total path optical thickness is the concern.

In comparing with the spherical case, we note from figure 7, the same general "flattening" of the source functions for lower optical thickness, and conversely, the increased curvature as the optical thickness increases. In all cases, the reflective curves are concave upward and the emissive curves are concave downward as they also are for the spherical case. It is evident from comparison with figure 5 and our earlier work in [1] that there are no qualitative differences between the plane layer solutions and the spherical solutions. In fact, there are very little quantitative differences at small optical thickness where all solutions converge to the first order result (i.e., curves are flat). At the higher optical thickness, however, the plane layer curves are significantly lower than for the spherical case as one might intuitively expect.

It turns out that there are relatively few cases where we can directly compare the source functions, *per se*, with results from the literature; however, there are extensive tables for comparing the integral properties such as reflectivity which we show in table 1 for the special case of normal incidence (i.e., $\mu=1$). The comparisons in table 1 all address the plane layer case using results from either the methodology of our previous work (labeled Ref. 1) or results from table 12 of the Van de Hulst text (labeled Ref. 4).

Table 1. Comparison of calculated reflectivities for normal incidence with plane layers.

REFLECTION

R(t,1)	wo=0.99		wo=0.80		wo=0.40		wo=0.20	
Tau	Ref. 1	Ref. 5	Ref. 1	Ref. 5	Ref. 1	Ref. 5	Ref. 1	Ref. 5
.03125	.03044	.03054	.02426	.02426	.01178	.01178	.00581	.00582
.06250	.05990	.05990	.04723	.04723	.02246	.02246	.01096	.01097
.12500	.11606	.11605	.08978	.08978	.04119	.04119	.01978	.01978
.25000	.21806	.21806	.16305	.16305	.07046	.07046	.03299	.03295
.50000	.38644	.38581	.27139	.27139	.10648	.10647	.04808	.04808
1.00000	.61602	.61602	.38439	.38437	.13056	.13055	.05637	.05636
2.00000	.82786	.82785	.41663	.41655	.11971	.11966	.04980	.04977
4.00000	.90228	.90221	.34105	.34079	.09234	.09221	.03847	.03841
8.00000	.85092	.85148	.29033	.28956	.08403	.08364	.03551	.03531

Before proceeding there are some potentially confusing circumstances that need to be cleared up when comparing with the Van de Hulst results. That is, in the Van de Hulst text, the "reflection" function, as we define it here, is separated into two components: one labeled transmission, $T(\tau, u)$, for general downward (sky-to-surface) diffuse propagation and another labeled reflection, $R(\tau, u)$, for general upward (surface-to-sky) diffuse propagation. This is a convention dating from early astrophysical studies based on planetary plane layers as viewed inward. Furthermore, the Van de Hulst transmission function includes a direct component, $e^{-\tau}$, that we need to subtract out to make the comparisons valid. One needs also to be cautioned that all results here pertain to Lambertian sources over the full 4π upper and lower hemispheres as the driving terms. That is, the relationship between our reflectivity, r_{acr} , and the Van de Hulst functions are as follows:

$$r_{acr}(\tau, u) = R(\tau, u) + T(\tau, u) - e^{-\tau} \quad (28)$$

where the $R(\tau, \mu)$ and $T(\tau, \mu)$ values are found under the heading of "Lambertian sources" in table 12 of the Van de Hulst text. We also note that the Van de Hulst tables refer to "intensities" referenced outward as calculated assuming unit input and are equivalent to our "normalized" source functions. The results here all pertain only to reflection since this is the only case reported in the Van de Hulst tables; however, there are some indirect graphical data for emission which we address later in this section.

Looking now at the numerical results of table 1, we see clearly that the comparisons between our work and Van de Hulst are quite favorable, showing discrepancies of less than 0.10 percent in almost all cases with the larger exceptions occurring only at the very highest optical depths where multiple scattering effects are most significant. Later studies verified that these disparities could be further diminished by using a higher spatial resolution in the numerical integrations, using a lower threshold for convergence, or both. Overall the results here are qualitatively similar to the spherical case, as one should expect. In particular, looking carefully at the numerical results of table 1 we see that all values tend to monotonically increase and reach a maximum somewhere between $\tau_0=2-4$ beyond which the values again decrease. This peak in the reflection curve is very similar to that found for the spherical case discussed in the previous section.

In passing, it also needs to be pointed out that the use of the analytical form of eq. (27) to perform the angular integrals was more of a necessity than a simple convenience because it turned out that the use of "brute force" numerical methods were extremely inefficient and in many cases required angular meshes on the order of milliradians to obtain the highest accuracies. This problem was of great practical concern and was completely resolved by using the Exponential Integrals of eq. (27). In any case, based upon the comparisons here there seems to be little doubt as to the validity of our approach—at least on matters pertaining to reflection.

In addressing the emissive case, Van de Hulst has taken the related approach, which we referred to as "embedded sources" in the discussion leading to eq. (15) in section 1. In this case there are no extensive tables with which to compare our results; however, Van de Hulst does give one graphical example demonstrating the angular dependence which we can relate to our case of reflection and emission. The relevant expressions for comparison in the plane layer case are as follows:

$$I_{\text{ref}}(\tau, u) = \int_0^{\tau_0} \hat{J}_{\text{ref}}[\tau_0, \omega_0; \tau'(z)] e^{-\tau'(z)/u} d\tau' \quad (29a)$$

$$I_{\text{emb}}(\tau, u) = \int_0^{\tau_0} \hat{J}_{\text{emb}}[\tau_0, \omega_0; \tau'(z)] e^{-\tau'(z)/u} d\tau' \quad (29b)$$

where u is the absolute value of the viewing angle cosine and z is vertical distance (fig. 6). The source functions are normalized to unity for the case of reflectivity and, equivalently, to a uniform unit embedded source for the case of emission as described by Van de Hulst.

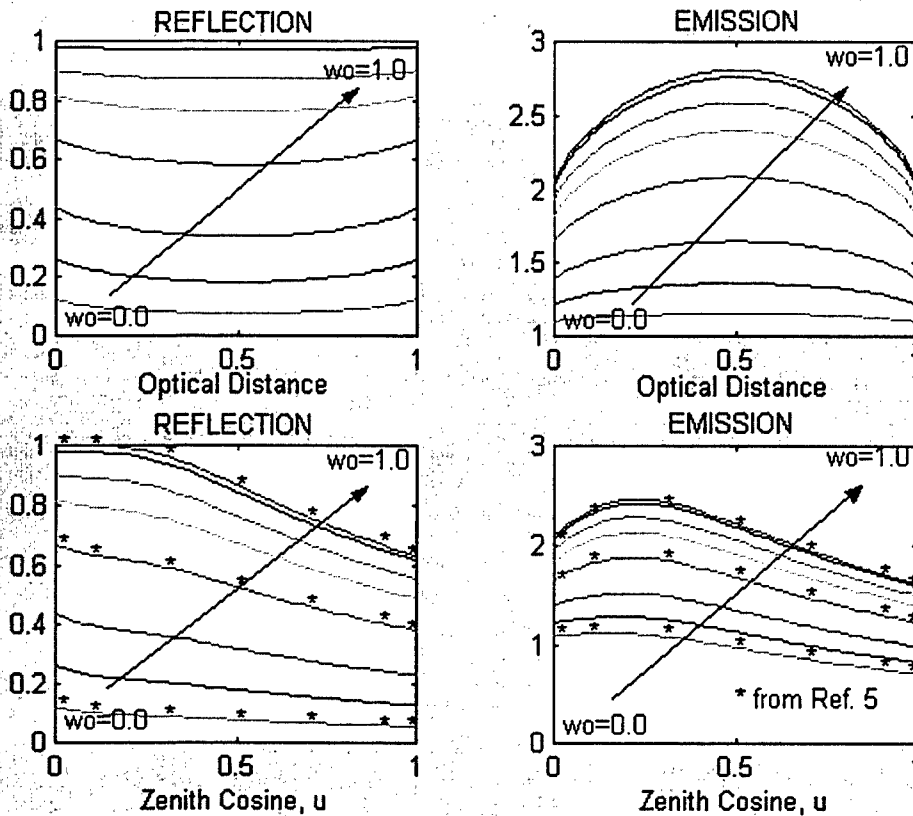


Figure 8. Relative intensity functions for plane layers: (a) reflectivity, (b) emission.

Results of comparisons for a single case ($\tau_0=1$) are shown in figure 8. The upper curves in figure 8 refer to the normalized source functions and are added here only for convenience to the reader; however, it should be noted that the emission functions here are not normalized to unity and that the ordering of the emissive curves are not inverted as they were for the case of (natural) thermal emission. This latter circumstance is due primarily to the absence of the prefactor $(1-\omega_0)$ in the definition of eq. (29b).

In the lower plots of figure 8 the abscissa for both cases is the slant path angle cosine, μ , and, as before, the various curves in each of the two subplots refer to cloud albedo. Note again that, as in the upper plots, the ordering of the curves for reflection and emission are the same; that is, both increase with increasing albedo. The smooth curves in figure 8 were all generated using the PILOT-EX methodology as modified to treat embedded sources. The discrete data points for the reflective case were obtained directly from the Van de Hulst tables using eq. (28) and those for emission were obtained directly from the plots of figure 9.14 in the Van de Hulst text.

For the reflective cases (lower left plots), it is significant that all curves exhibit a monotonic decrease in reflectivity as the zenith angle cosine increases. For example, in the conservative case, the curve begins with a value identically equal to unity at $u=0$ (horizontal propagation) and eventually decreases to a value of around 0.610 at $u=1$ (vertical propagation). This general behavior is characteristic of all curves and should be expected since, according to eq. (26), the slant path optical thickness (τ/u) approaches infinity as u approaches zero and decreases as the

slant angle decreases. As the albedo decreases, the curves all decrease in magnitude and tend to "flatten" and become nearly independent of angle at the lowest albedo.

For the emissive cases (lower right plots), the curves are similar to the reflective case in general behavior except for the curious maxima that occur in the proximity of $\mu=0.2$ [$\theta=78^\circ$] which is most pronounced at the higher albedos. Again, as the albedo decreases the curves tend to decrease in magnitude and flatten out as was also seen for reflective case. Although it may not be obvious from the plots it does turn out to be a fact that the embedded source results can be related to emissivity through a scaling factor of the form $(1-\omega_0)$. We have made use of this fact in table 2 where we again summarize results in numerical form for both the reflective and emissive cases.

Table 2. Comparison of calculated reflectivities and emissivities for various slant angles.

REFLECTION

R(t,1)	wo=.99		wo=.80		wo=.40		wo=.20	
u	Ref. 1	Ref. 5	Ref. 1	Ref. 5	Ref. 1	Ref. 5	Ref. 1	Ref. 5
.00010	.97924	.97960	.66525	.66973	.26169	.26639	.12012	.12286
.10000	.97676	.97675	.63523	.63518	.23206	.23272	.10331	.10329
.30000	.94032	.94032	.59302	.59300	.20536	.20534	.08941	.08940
.50000	.84281	.84281	.52782	.52778	.18048	.18046	.07815	.07814
.70000	.74104	.74103	.46300	.46298	.15765	.15763	.06814	.06813
.90000	.65373	.65373	.40804	.40803	.13868	.13867	.05989	.05988
1.00000	.61602	.61602	.38439	.38437	.13056	.13055	.05637	.05636

EMISSION

E(t,1)	wo=.99		wo=.80		wo=.40		wo=.20	
u	Ref. 1	Ref. 5	Ref. 1	Ref. 5	Ref. 1	Ref. 5	Ref. 1	Ref. 5
.00010	.02075	.02040	.33475	.33027	.73831	.73361	.87988	.87714
.10000	.02320	.02320	.36473	.36477	.76790	.76723	.89664	.89666
.30000	.02400	.02401	.37130	.37133	.75896	.75899	.87492	.87493
.50000	.02185	.02185	.33685	.33688	.68418	.68420	.78652	.78652
.70000	.01931	.01932	.29734	.29737	.60270	.60272	.69221	.69222
.90000	.01707	.01708	.26276	.26278	.53213	.53214	.61092	.61093
1.00000	.01610	.01610	.24773	.24775	.50156	.50157	.57575	.57576

In table 2, the upper set refers to reflectivity and lower set refers to emissivity using either our methodology and eq. 28 or the angular dependent tables of Van de Hulst. The study variables in this case are the slant angle and albedo for a single cloud optical thickness of unity. Examination of the results again show near perfect agreement with the largest errors occurring at the lowest angles which is a result we may expect due to the very high slant value optical thickness, which complicates the multiple scattering solutions.

Taken together, the comparisons here for both reflection and emission are favorable and strongly support the validity of our approach. We have other anecdotal and qualitative evidence from the literature on both cylinders and optically thick spheres that also tend to support our conclusions, but nothing as extensive as the Van de Hulst study.

6. Bandpass Functions and Apparent Temperature

It has been assumed throughout that the bandpass functions introduced in [1] take care of all the conversions from temperature to (thermal) radiance and vice versa. That is, for any real, calibrated, radiometric measurement, in the absence of any emissive or obscuring effects, the sensor signal responds in accordance with the following expression:

$$B_{\Delta\lambda}^*(T) = \frac{\int_0^{\infty} f_{\Delta\lambda}(\lambda) B(\lambda, T) d\lambda}{\int_0^{\infty} B(\lambda, T) d\lambda} \left(\frac{\sigma T^4}{\pi} \right) = F_{\Delta\lambda}^*(T) \frac{\sigma T^4}{\pi} \quad (30)$$

where λ is the wavelength within the specified window, $\Delta\lambda$, and $f_{\Delta\lambda}(\lambda)$ represents some specified instrument bandpass "filter" function. Other quantities are the Stefan Boltzman constant, σ , the (absolute) real thermodynamic temperature of the target surface, T , and the Planck Blackbody function, $B(\lambda, T)$. For an infrared sensor, eq. (30) produces a one-to-one correspondence between sensor signal and surface temperature, provided that the underlying "target" is a Blackbody of uniform temperature and there are no intervening emissive, atmospheric, or obscurant effects.

To illustrate, in figure 9, we show plots of eq. (30) for several idealized bandpass functions of practical interest, including the full spectrum case, [i.e., $f_{\Delta\lambda}(\lambda) \equiv 1$ for all λ], for which the expression reduces to the familiar Stefan-Boltzman Equation [i.e., $B_{\infty}^*(T) = \sigma T^4 / \pi$].

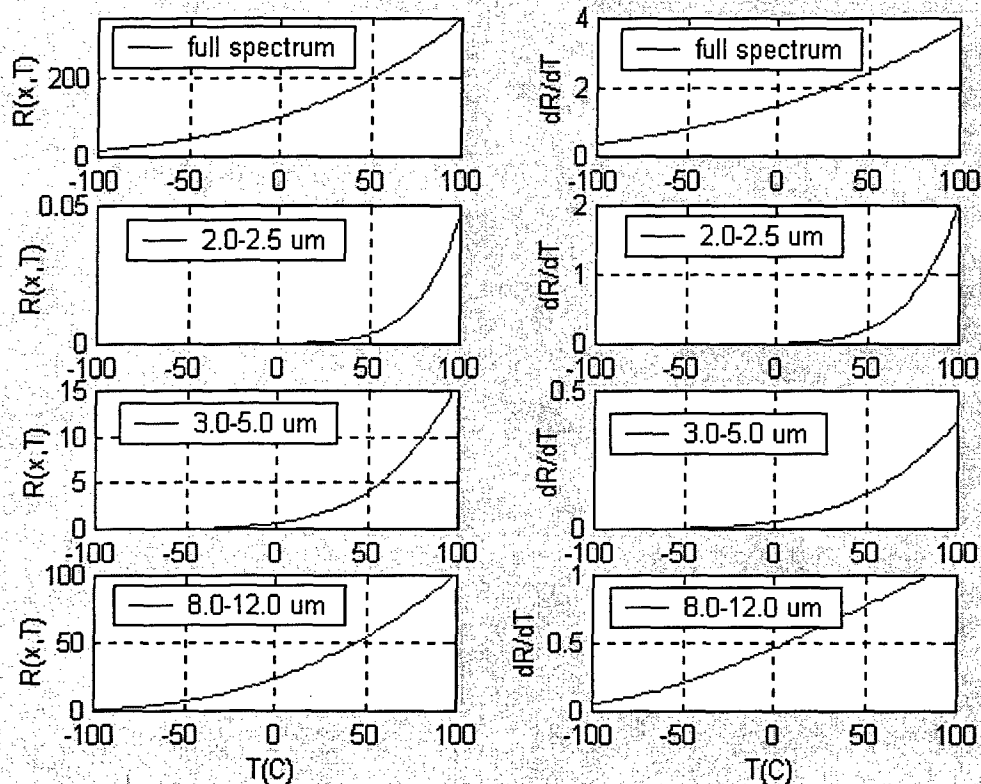


Figure 9. Bandpass functions: radiance, left; thermal derivative, right.

In making the plots of figure 9 we have modeled the filter function, $f_{\Delta\lambda}(\lambda)$ as an idealized unit rectangular step function over the specified window ($\Delta\lambda$), as indicated on the figures. The plots on the left are the bandpass functions and those on the right are the corresponding "thermal" derivatives used in defining the "radiation contrast" that will be explained more fully in a later section. In all cases, the mathematical calculations were performed using the semi-analytical methods described in the SPIE (International Society for Optical Engineering) Handbooks [9] and are accurate to within 0.01 percent for the range of temperatures shown. For ease of explanation we have assumed that the idealized instrument has been calibrated against a Blackbody target so that any instrumental artifacts are either compensated or otherwise removed [10]. Thus, with an instrument so calibrated, it is possible, in principle, to convert the measured signal to the target temperature using the inverse of eq. (30), or graphically using the plots. Conversely, if we know the target temperature, we can immediately determine the corresponding radiance using either the graphs or eq. (30) in the forward mode. Thus we can think of the plots as a "calibration" function for converting radiometric measurements to temperature and vice versa as long as the "targets" are blackbodies and there are no intervening atmospheric or aerosol effects.

To include the effect of a "hard target" emissivity, the conventional approach is to define an "apparent" temperature [11] such that the total energy in the bandpass is the same as that in the reduced signal. That is, we form the following "energy balance," accounting for both direct emissions from the target and any reflections from the ambient surroundings, as

$$\int_0^{\infty} f_{\Delta\lambda}(\lambda) B(\lambda, T_{\text{tgt}}^*) d\lambda = \epsilon_{\text{tgt}} \int_0^{\infty} f_{\Delta\lambda}(\lambda) B(\lambda, T_{\text{tgt}}) d\lambda + r_{\text{tgt}} \int_0^{\infty} f_{\Delta\lambda}(\lambda) B(\lambda, T_{\text{ext}}^*) d\lambda \quad (31)$$

where T_{tgt}^* is defined as the “apparent” target temperature and T_{tgt} is the corresponding real (i.e., thermodynamic) target temperature. Other terms in eq. (31) are the target emissivity, ϵ_{tgt} , the target reflectivity, r_{tgt} , and the apparent ambient temperature, T_{ext}^* , which determines the magnitude of incoming irradiance from the ambient (sky and surface) surroundings. Note that here and throughout we adopt a notation wherein the superscript (*) denotes apparent temperature.

Ignoring reflections for the moment, it is clear that the effect of emissivity is to cause a *uniform* signal reduction across the spectrum and is quite different than that of changing the temperature which actually causes a *non-uniform* change in the underlying spectrum as well as a reduction in the overall signal magnitude. The situation is illustrated in figure 10 where we have plotted a series of spectra corresponding to various apparent temperatures on the left and the corresponding energy equivalent spectra of the emissive counterparts on the right. For convenience we use the “full spectrum” relationship (i.e., $T_{\text{app}} = \epsilon^{1/4} T_{\text{real}}$).

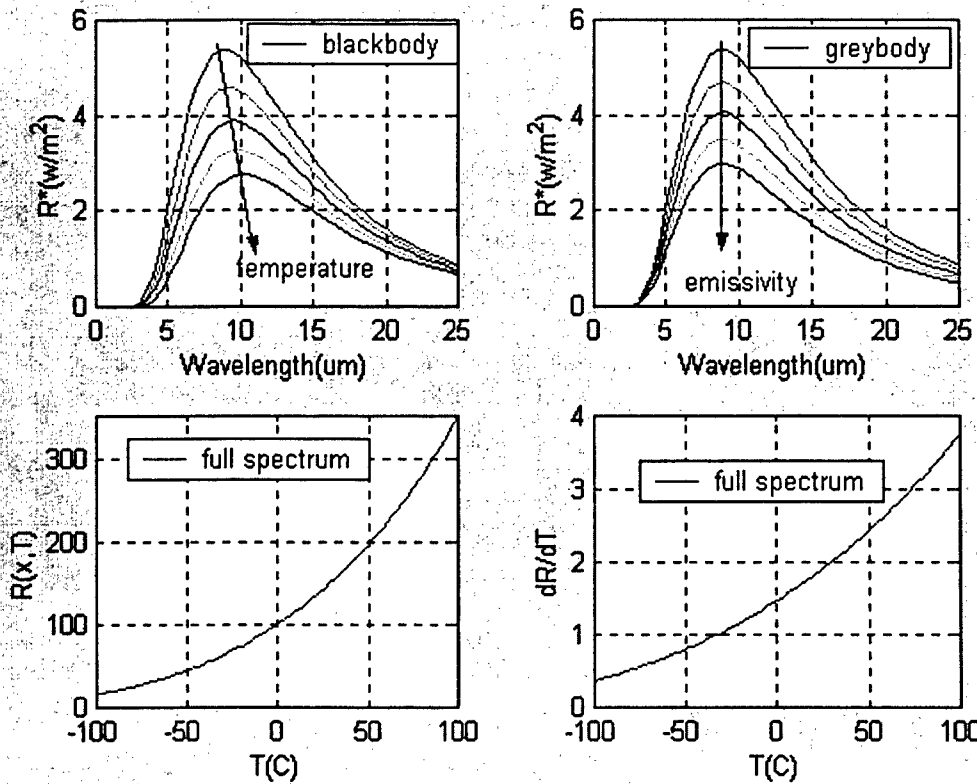


Figure 10. Spectral plots to demonstrate concept of apparent temperature.

A subtle but significant difference in the two sets of curves is the shift of the maximum to longer wavelengths in the left set but a simple multiplicative effect for each curve on the right set. This inconsistency is a consequence of the definition of apparent temperature that can cause problems

in applications where it is critical to determine the actual value of the (real) temperature. For our application however, we are ultimately concerned only with measured radiant energies for which this inconsistency is not a major concern.

The question now arises as to how to treat the received signal in the presence of an obscuring aerosol which we assume can either reduce or enhance the received signal due to the actions of extinction, emission, and ambient in-scatter plus the possibility that the cloud, background, and target temperatures may all be different. Ignoring for the moment, the effects of emission and scattering, it is clear that the effect of direct (Beers's Law) signal attenuation can be treated by extending the usual definition to include a further signal reduction in the "energy balance" relationship as follows:

$$\int_0^{\infty} f_{\Delta\lambda}(\lambda) B[\lambda, T_{tgt}^*(\tau)] d\lambda = t_{aer}(\tau) \left\{ \int_0^{\infty} f_{\Delta\lambda}(\lambda) \epsilon_{tgt} B(\lambda, T_{tgt}) d\lambda + \int_0^{\infty} f_{\Delta\lambda}(\lambda) r_{tgt} B[\lambda, T_{ext}^*] d\lambda \right\} \quad (32)$$

where $t_{aer}(\tau) [=e^{-\tau}]$ is the cloud transmissivity and, $T_{tgt}^*(\tau)$ is the target apparent temperature as sensed through an obscurant of optical thickness (τ) and, for the moment, accounting only for the direct attenuation. Thus, the treatment for transmittance is similar to that for "hard target" emissivity and the combined effect of both is multiplicative. Note, too, that this "apparent" target temperature is the radiative temperature that would actually be sensed by an instrument calibrated against a Blackbody.

The inclusion of the effects of the aerosol emissivity and reflectivity is treated independently, but in a similar manner. That is, accounting for the total diffuse (path) radiance from the cloud, we form the appropriate energy balance to define the apparent cloud temperature, $T_{cld}^*(\tau)$, analogous to the apparent target temperature, as follows:

$$\int_0^{\infty} f_{\Delta\lambda}(\lambda) B[\lambda, T_{cld}^*(\tau)] d\lambda = \epsilon_{aer}(\tau) \int_0^{\infty} f_{\Delta\lambda}(\lambda) B(\lambda, T_{cld}) d\lambda + r_{aer}(\tau) \int_0^{\infty} f_{\Delta\lambda}(\lambda) B[\lambda, T_{ext}^*] d\lambda \quad (33)$$

where $\epsilon_{aer}(\tau)$ and $r_{aer}(\tau)$ are, respectively, the aerosol emissivity and reflectivity as defined in previous sections, T_{cld} is the real (thermodynamic) temperature of the cloud, and T_{ext} remains as defined in eq. (31). Note that the above expression defines the apparent cloud temperature only, not including the "target" contribution.

We now define the composite apparent temperature as affected by all processes by adding contributions from both the (attenuated) target signal (eq. 32) and cloud radiance (eq. 33) and thus obtain, for the total energy balance, the following:

$$\int_0^{\infty} f_{\Delta\lambda}(\lambda) B[\lambda, T_{mea}^*(\tau)] d\lambda = \int_0^{\infty} f_{\Delta\lambda}(\lambda) B[\lambda, T_{tgt}^*(\tau)] d\lambda + \int_0^{\infty} f_{\Delta\lambda}(\lambda) B[\lambda, T_{cld}^*(\tau)] d\lambda \quad (34)$$

where we explicitly assert that the apparent temperature in this case represents the actual “measured” radiometric temperature, $T_{\text{mea}}(\tau)$, as would be sensed by a real instrument. This assertion, which may appear at first glance as a leap of faith, is clarified by realizing that the whole derivation is based on a careful treatment of the energy balance at each step using what we assume to be “measured” data.

Up to this point, we summarize by expanding and rewriting eq. (34) more conveniently in terms of the bandpass functions of eq. (30) as follows:

$$B_{\Delta\lambda}^*[T_{\text{mea}}^*(\tau)] = t_{\text{aer}}(\tau)B_{\Delta\lambda}^*(T_{\text{tgt}}^*) + \varepsilon_{\text{aer}}(\tau)B_{\Delta\lambda}^*(T_{\text{cld}}) + r_{\text{aer}}(\tau)B_{\Delta\lambda}^*(T_{\text{ext}}^*) \quad (35)$$

where T_{tgt}^* is the target apparent temperature determined via eq. (31). At this point it should be made clear that, for a given instrument specification, all terms on the right side of eq. (35) can be obtained directly from calibration curves such as those of figure 10 (or equivalent from numerical look up tables) using the known temperatures and the calculated aerosol properties. The sum of all terms then gives the full signal radiance from which the apparent, or “measured,” temperature can be obtained by inverting the process with the same calibration curve. Alternatively we can express this intuitive process formally as,

$$T_{\text{mea}} = B_{\Delta\lambda}^{*(-1)}(R_{\text{mea}}) \quad (36)$$

where

$$R_{\text{mea}} = t_{\text{aer}}(\tau)B_{\Delta\lambda}^*(T_{\text{tgt}}^*) + \{\varepsilon_{\text{aer}}(\tau)B_{\Delta\lambda}^*(T_{\text{cld}}) + r_{\text{aer}}(\tau)B_{\Delta\lambda}^*(T_{\text{ext}}^*)\}$$

where the superscript (-1) represents the inverse of the function and all other quantities have been identified in the previous paragraphs. As usual, the first term on the right side of eq. (36) is the direct contribution and the second (bracketed) term is the diffuse contribution (also called the path radiance in applications).

We now work an example using the hypothetical data of table 3 assuming, for convenience, a “full spectrum” bandpass and a cloud total optical thickness of unity (i.e., $t_{\text{aer}} = e^{-1} = 0.368$).

Table 3. Hypothetical data for bandpass example.

EXAMPLE $\tau=1.0$		units = watt/m ² Sr ⁻¹	
$t_{\text{aer}}=0.368$	$T_{\text{cld}}=40^\circ\text{C}$	$B_{\text{cld}}=173$	$t_{\text{aer}}*B_{\text{cld}}=63.9$
$\varepsilon_{\text{aer}}=0.421$	$T_{\text{ext}}^*=10^\circ\text{C}$	$B_{\text{ext}}=116$	$\varepsilon_{\text{aer}}*B_{\text{ext}}=48.8$
$r_{\text{aer}}=0.211$	$T_{\text{tgt}}^*=20^\circ\text{C}$	$B_{\text{tgt}}=133$	$r_{\text{aer}}*B_{\text{tgt}}=28.1$
$R_{\text{mea}}=140.8$			

In table 3, the first two columns of data are the raw input that we have arbitrarily “made up” for the example and the data in the remaining two columns are calculated using the methods described above. The first step in the example is to calculate the fractional radiance, $B_{\Delta\lambda}^*(T)$, for each of the three components. The computations can be done either graphically from the upper leftmost plot of figure 9 or, since we are addressing the full spectrum bandpass, from the Stefan-Boltzman analytical expression. In either case the results are as shown in the third column of table 3. The data in fourth column represent the products of column 1 and column 3 which give

each of the three terms on the right side of eq. (36). The resultant total measured radiance is found by summing the final column, which yields a value of 140.8 (watt/m² Sr⁻¹) from which we derive an apparent temperature of 24.1 °C by the inverse procedure. Note from the example that if we had ignored the path radiance contributions, the resultant radiance of 63.9 watt/m² Sr⁻¹ would correspond to an apparent temperature of -29.2 °C, producing an error of -73.3 °C, which is significant in most applications.

7. Radiation Contrast (Thermal Derivative)

It turns out that scanning systems such as a FLIR (forward-looking infrared) imager are not designed to rely upon the magnitude of a sensed signal, *per se*, but instead utilize the concept of “ac coupling” which is based upon sensing incoming signal differences, or contrast. In the analysis of these type systems it is usual to address the case wherein the sensed temperature differences, ΔT , are small enough so that we can use the following linear expansion:

$$I(T + \Delta T) = I(T) + \frac{dR}{dT} \Delta T \quad (37)$$

where $I(T)$ and $I(T + \Delta T)$ represents two measured signals received from adjacent scene “pixels” and $R[=R(\Delta\lambda, T)]$ will later be identified with the band weighted blackbody function of eq. (30). Upon rearranging eq. (37), we come about the definition for radiation contrast [9], $C_r(T)$, or what actually amounts to the thermal derivative, that is [11],

$$C_r(T) = \frac{I(T + \Delta T) - I(T)}{\Delta T} = \frac{\Delta I}{\Delta T} \approx \left. \frac{dR}{dT} \right|_{T=T_{mea}} \quad (38)$$

where we have taken care to point out and make explicit that the thermal derivative is to be evaluated at the measured temperature, T_{mea} (i.e., the apparent “temperature” that the receiver actually senses), and must include the full effect of any intervening aerosols, including path radiance. For our application, the thermal derivative can be evaluated directly from eq. (36); that is, generalizing somewhat we have

$$\left. \frac{dR}{dT} \right|_{T_{mea}} = t_{aer}(\tau) \left. \frac{dR_1}{dT} \right|_{T_{mea}} + \epsilon_{aer}(\tau) \left. \frac{dR_2}{dT} \right|_{T_{mea}} + \tau_{aer}(\tau) \left. \frac{dR_3}{dT} \right|_{T_{mea}} \quad (39)$$

where, for our application, we will eventually replace the R functions with the fractional blackbody functions of eq. (30). Our point in writing eq. (39) as such is to make it clear that if the *functional forms* of R_1 , R_2 , and R_3 are the same, then the three derivatives are all the same since they are all evaluated at the same point, T_{mea} . Thus, when actually applied to eq. (36) we have

$$\begin{aligned} \left. \frac{dR}{dT} \right|_{T_{mea}} &= \{t_{aer}(\tau) + \epsilon_{aer}(\tau) + r_{aer}(\tau)\} \left. \frac{dB_{\Delta\lambda}^*(T)}{dT} \right|_{T_{mea}} \\ &= \left. \frac{dB_{\Delta\lambda}^*(T)}{dT} \right|_{T_{mea}} \end{aligned} \quad (40)$$

where in writing the last expression we have used the continuity condition $[\epsilon(\tau) + r(\tau) + t(\tau) = 1]$ of eq. (25) and, as before, $B^*(T)$ is the bandpass function appropriate for the particular system under consideration. Some plots of the radiation contrast for various bandpasses of interest were presented earlier in the rightmost plots of figure 9. It is worth emphasizing that eq. (38) applies to the situation where the contrast is small and should not be used for situations where the contrast is large (in which case the target is usually obvious anyway).

The impact of the radiation contrast on the actual "sensed" temperature difference can be determined by combining the definition of eq. (38) with eq. (40) to obtain

$$(\Delta I)_{mea} = \left. \frac{dB_{\Delta\lambda}^*(T)}{dT} \right|_{T_{mea}} (\Delta T)_{mea} = C_R(T_{mea})(\Delta T)_{mea} \quad (41)$$

where $(\Delta I)_{mea}$ represents the measured ac signal difference, and $(\Delta T)_{mea}$ is the corresponding equivalent temperature difference. It is also useful to apply a form of eq. (41) to the system noise (radiance) signal, ΔR_{sys} , to produce

$$\Delta R_{sys} = C_R(T_n) \Delta T_n \quad (42)$$

where ΔT_n is called the "noise equivalent" temperature differential commonly used in hardware systems analysis.

We now see an immediate problem for the analyst because the exact measured temperature, T_{mea} , is not necessarily known for these types of system since only differences are considered. Nevertheless, the concept of sensing contrast directly is an attractive alternative in applications because there is at least a partial mitigation of the (usually unfavorable) effects of path radiance which comes about by differencing (see section 7). It is interesting to note, however, that the effect of path radiance on radiation contrast can be to enhance the sensitivity. This can be seen from the rightmost plots of figure 9 where it is clear that the radiation contrast, and thus the system sensitivity, generally increases as the sensed temperature increases. However, this is not the complete story since we have yet to examine the effect of aerosol induced noise, which we will consider in the next section.

8. Effect of Aerosol-Induced Noise

As noted in the previous section, in modeling the performance of an ac coupled system such as the FLIR, the received radiance can be modeled as the difference between two successive samples from adjacent pixels, and one of the relevant parameters affecting system performance is the signal-to-noise ratio, which we will derive in this section. In this case the incident "signal" in the presence of an intervening aerosol is modeled as

$$\Delta I(\tau_1, \tau_2) = [R(\tau_1, T_{1,mea}) - R(\tau_2, T_{2,mea})] \quad (43)$$

which represents the difference in the measured radiance between two adjacent "pixels" labeled by subscripts "1" and "2." Applying eq. (36) twice for the two pixels in question immediately yields

$$\Delta I(\tau_1, \tau_2) = [e^{-\tau_1} B_{\Delta\lambda}^*(T_{1,tgt}^*) - e^{-\tau_2} B_{\Delta\lambda}^*(T_{2,tgt}^*)] + [R(\tau_1, T_{1,dif}) - R(\tau_2, T_{2,dif})] \quad (44)$$

where we have arranged terms such that the first bracketed expression is the direct contribution to the differential signal (i.e., ΔR_{dir}) and the second represents the aerosol diffuse contribution (i.e., ΔR_{dif}), also called the path radiance.

We next follow the usual development by invoking the following approximations:

$$\begin{aligned} \tau_1 &\cong \tau_2 \approx \tau \\ T_{1,dif} &\cong T_{2,dif} \approx T_{dif} \end{aligned} \quad (45)$$

both of which may usually be justified because the two pixels are adjacent so that the optical paths through the atmosphere are nearly the same. Applying the above approximation to eq. (44) yields

$$\begin{aligned} \Delta I(\tau_1, \tau_2) &= e^{-\tau} [B_{\Delta\lambda}^*(T_{1,tgt}^*) - B_{\Delta\lambda}^*(T_{2,tgt}^*)] + [R(\tau_1, T_{1,dif}) - R(\tau_2, T_{2,dif})] \\ &= [e^{-\tau} B_{\Delta\lambda}^*(T_{1,tgt}^*) - B_{\Delta\lambda}^*(T_{2,tgt}^*)] + [\Delta R_{aer}(\tau, T_{dif})] \end{aligned} \quad (46)$$

where the second bracketed expression, $\Delta R_{aer}(\tau, T_{dif})$, represents the path radiance (difference) contribution which, owing to the approximations of eq. (45), is assumed to be small but not necessarily zero and not necessarily small with respect to the direct term. It is natural to take the first bracketed term in eq. (46) to be the true difference *signal* (i.e., derived from that part of the received radiance that actually originated from the target) and the remainder is taken as *noise*. Thus, the signal to noise ratio becomes

$$\text{SNR}(\tau) = \frac{e^{-\tau} [B_{\Delta\lambda}^*(T_{1,\text{tgt}}^*) - B_{\Delta\lambda}^*(T_{2,\text{tgt}}^*)]}{\Delta R_{\text{aer}}(\tau, T_{\text{dif}}) + \Delta R_{\text{sys}}} \quad (47)$$

where we have also added a term, ΔR_{sys} , to include any noise contribution from the system hardware as is common in “clear air” studies more often addressed in the literature [11]. It is often tempting to assume that the path radiance contributions either cancel each other, or at least the difference is small compared to the direct term in which case the aerosol noise term can be neglected. At certain extremes this is a valid assumption and a case that we will address later; however, in general, it is more reasonable to assume the aerosol contribution to be proportional to the (average) value of the magnitude of the path radiance. Thus for later reference we write

$$\Delta R_{\text{aer}}(\tau, T_{\text{dif}}) \propto \frac{\{R(\tau, T_{1,\text{dif}}^*) + R(\tau, T_{2,\text{dif}}^*)\}}{2} = \delta_w R(\tau, T_{\text{dif}}) \quad (48)$$

where δ_w is an *ad hoc* “weather” dependent parameter which we conjecture can range from a value of zero for low turbulence conditions to a value on the order of unity for high turbulence conditions. Clearly, the path radiance in eq.(48) can be written in terms of the aerosol cloud properties as

$$R(\tau, T_{\text{dif}}^*) = \epsilon_{\text{aer}}(\tau) B_{\Delta\lambda}^*(T_{\text{cld}}) + r_{\text{aer}}(\tau) B_{\Delta\lambda}^*(T_{\text{ext}}^*) \quad (49)$$

where T_{cld} is the cloud temperature, and T_{ext}^* is the ambient radiative temperature, as defined in connection with eq. (36) of the previous section.

Continuing with the usual development, we next invoke the “small signal” approximation which amounts to assuming that the underlying direct signal difference is small enough such that eq. (38) of the previous section holds. In this case we can replace the radiance differentials in the numerator of eq. (47) with their corresponding apparent temperature differentials as follows:

$$B_{\Delta\lambda}^*(T_{1,\text{tgt}}^*) - B_{\Delta\lambda}^*(T_{2,\text{tgt}}^*) \approx C_r(T_{\text{mea}})(T_{1,\text{tgt}}^* - T_{2,\text{tgt}}^*) \quad (50)$$

where $C_r(T_{\text{mea}})$ is the thermal derivative defined by eq. (41) in the previous section and is evaluated at the measured apparent temperature which we will ultimately take as the average of the two target pixels.

Making the obvious substitutions in eq. (47), we now have

$$\text{SNR}(\tau) = \frac{e^{-\tau} C_r(T_o)(\Delta T)_o}{\delta_w R(\tau, T_{\text{dif}}^*) + C_r(T_n)\Delta T_n} \quad (51)$$

where we have also used the thermal derivative, $C_r(T_n)$, to convert the system noise, R_{sys} , from a radiance-based parameter to a noise equivalent temperature difference, ΔT_n , as it is commonly

done in systems analysis [cf., eq. (42)]. We have also substituted T_o for the average apparent temperature [i.e., $T_o = (T_{1,tgt} + T_{2,tgt})/2$] and ΔT_o as the corresponding temperature differential (i.e., $\Delta T_o = T_{1,tgt} - T_{2,tgt}$).

Finally, collecting all terms and making all of the suggested substitutions, we have

$$SNR(\tau) = \left\{ \frac{e^{-\tau} B_{\Delta\lambda}^*(T_o)}{\delta_w R(\tau, T_{dif}^*) + C_r(T_n) \Delta T_n} \right\} \left\{ \frac{C_r(T_o) (\Delta T)_o}{B_{\Delta\lambda}^*(T_o)} \right\} \quad (52)$$

where, for convenience, we have multiplied both numerator and denominator by the average target radiance, $B_{\Delta\lambda}^*(T_o)$. Written as such the second bracketed term in eq. (52) represents the surface level (i.e., unobscured) radiance based contrast at the target surface (i.e., $\Delta R_o/R_o$) and the first bracketed term represents a generalized version of what is sometimes called the "contrast transmission," the reciprocal of which, for historical reasons, is referred to in the older literature as the "sky-to-ground" ratio (although the terminology is somewhat inappropriate here).

In the limit where the aerosol noise can indeed be neglected either because conditions are such that the parameter, δ_w , is small or because the system noise, ΔR_{sys} , is relatively large, eq. (52) reduces to the commonly accepted "clean air" form given by

$$SNR(\tau)_{\Delta R_{sys} \rightarrow 0} = e^{-\tau} \frac{\Delta T_o}{\Delta T_n} \quad (53)$$

where we have assumed that the temperatures for the signal and system noise are sufficiently close that the thermal derivatives are the same (i.e., $T_o \sim T_n$), an assumption which requires some care and attention in real applications.

Another example for which we have some interest is the case of thermal equilibrium between the cloud and the ambient atmosphere (i.e., $T_{cld} = T_{ext}$) in which case, neglecting the system noise term, the contrast transmission, T_{con} , becomes

$$T_{con}(\tau) = \left\{ \frac{e^{-\tau}}{1 - e^{-\tau}} \right\} \left\{ \frac{B_{\Delta\lambda}^*(T_o)}{B_{\Delta\lambda}^*(T_{cld})} \right\} \quad (54)$$

where we have also used the general condition for isothermal clouds [$\varepsilon(\tau) + r(\tau) = 1 - e^{-\tau}$] from eq. (25). For the full equilibrium case (i.e., $T_{tgt} = T_{cld} = T_o$), eq. (54) reduces to the well-known classical result $[(1 - e^{-\tau})/e^{-\tau}]$, which is often used for plane layers. Thus it appears that the development here ties together several often used approximations and offers a way to bridge the various extremes. The problem at the moment is that the form of the *ad hoc* weather dependent parameter, δ_w , is not known and does not, at this period in time, appear to be tractable theoretically. We do have an ongoing experimental effort based on (near) simultaneous field measurements of path radiance and transmittance to shed some light on this issue [13].

9. Temperature Stratification

In this section we extend the study to include temperature stratification in the emissive cloud formulation. The extension is reasonably straightforward except that the definition of the cloud emissivity is no longer consistent with basic physical principles as it was for the isothermal case. However, this is only a minor problem that we circumvent by defining a “practical” emissivity normalized to the maximum which, if used consistently, causes no real problem in applications of our type. Also, for the non-isothermal case, the emissive source functions no longer mirror the inverse of the reflective source functions as they did for the isothermal case and therefore the general expression relating emissivity to reflectivity [eq. (25)] is no longer valid and other fundamental notions need to be modified. However, no real conceptual difficulties exist in actually applying the method, but the treatment is somewhat less elegant and the results a bit more complex.

As before, the underlying equation is the thermal version of the radiative transfer equation which, for reasons cited above, we normalize, in first order, as follows:

$$J_{\text{dir}}(\tau_o, \omega_o; \tau) = \frac{(1 - \omega_o)}{B_{\Delta\lambda}^*(T_{\text{max}})} \int_0^\tau B_{\Delta\lambda}^*[T_{\text{cld}}(r)] e^{-\tau'(\tau_o, \tau')} d\tau' \quad (55)$$

where τ_o and ω_o are, respectively, the cloud total optical thickness and albedo, τ is the optical thickness referenced to zero at the edge of the cloud (see sec. 2) and T_{max} is the maximum cloud temperature which, for our hotter-than-ambient Gaussian clouds, will come about at the cloud center.

The cloud temperature, $T_{\text{cld}}(r)$, is the aerosol real (thermodynamic) temperature at a radial distance, r , from the cloud center and is modeled in our standard Gaussian cloud as

$$T_{\text{cld}}(r) = T_{\text{amb}} + \rho_{\text{mix}}(r)(T_{\text{max}} - T_{\text{amb}}) \quad (56)$$

where T_{amb} is the ambient temperature outside the cloud and $\rho_{\text{mix}}(r)$ is a “mixing factor” taken as proportional to the aerosol concentration normalize to unity at the cloud center [i.e., $\rho_{\text{mix}}(r) = C(r)/C_o$] and where the aerosol concentration, $C(r)$, is modeled in accordance with the procedures described in section 2. It is clear from inspection that eq. (56) yields a maximum value, T_{max} , at the cloud center and drops to near ambient, T_{amb} , at the cloud edge. It is furthermore clear that the overall radial symmetry is preserved so that the multiple scattering methodology described in our previous report remains valid; thus, we can calculate the multiple scattering source function iteratively using eq. (55) as the initial condition. Some examples of thermally stratified emissive source functions are shown in figure 11 for a variety of cloud-to-ambient temperature differentials.

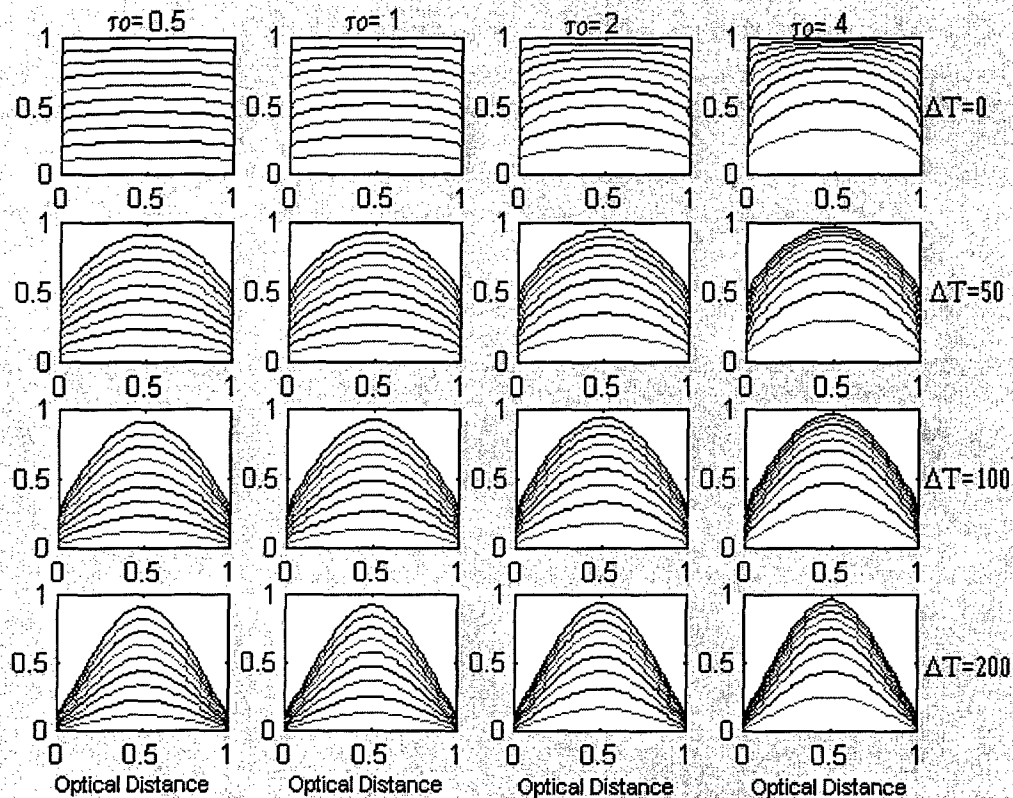


Figure 11. Emissive source functions for non-isothermal clouds.

In figure 11, the first row of subfigures represents the isothermal case which is identical to the corresponding plots of figure 7 but which we repeat here for reference. The remaining three rows correspond to the various temperature differentials $[\Delta T = T_{\max} - T_{\text{amb}}]$ as indicated to the right of each row. Each of the four columns correspond to a different cloud optical thickness ranging from $\tau_0 = 0.50$ to 4.0 as indicated at the top of each column. Each subplot, of which there are 16 total, includes 11 curves (9 discernable) corresponding to different values of albedo increasing in equal increments from $\omega_0 = 0$ (extreme top) to $\omega_0 = 1$ (extreme bottom) following the usual monotonic scheme used throughout.

In studying the rows and columns of figure 11, two general trends are immediately apparent as manifested by the increased curvature, or "narrowing," of the curves as either the optical thickness increases (along each row) or as the temperature differential increases (down each column). There is also a small but noticeable increase in the magnitude of the source function with increasing optical thickness, which seems to be most marked at the higher albedos represented by the lower-lying curves in each subplot. The effect of increased temperature has little effect on the magnitude of the source functions except at the cloud edges where the magnitude clearly decreases with increasing temperature differential, a behavior due primarily the normalization convention. The results support the assumption of a strong build up of internal radiance in the center as the temperature differential is increased. From the trends shown, we anticipate that the curves continue to narrow, as the temperature differential increases, and eventually collapse to near delta functions at the extreme, especially at the higher values of optical thickness.

The general behavior of the source functions, most noticeably the build up of source radiance in the cloud interior, suggests that the effect will, in turn, correspond to a lowering of the emissivity. This is intuitively plausible because any source at the cloud center will necessarily experience some "self extinction" in reaching the cloud exterior. Thus, we would expect the calculated emissivities to become lower and lower as the temperature differential increases and become more and more pronounced as the optical thickness increases. Some of our preliminary calculations have borne this out; in particular we have found emissivity ratios $[\epsilon(\Delta T=x)/\epsilon(\Delta T=0)]$ to be on the order of 52 percent for an optical thickness of $\tau=1$ and on the order of 40 percent for an optical thickness of $\tau=4$, and in both cases an albedo of $\omega_0=0.50$. Unfortunately, we have not yet found a way to present the results in a systematic way, but this is a viable goal for further work. We have also looked at some data on emissive sources and do have evidence that self extinction occurs in real smokes [15].

10. Summary

The details given here along with those also given in our companion paper [1] offer a complete solution to the radiative transfer equation for finite aerosol clouds of radial symmetry. The method addresses both aerosol thermal emission as well as reflection, including all orders of multiple scattering. The method represents exact solutions that compare favorably with other studies when applied to plane layers. We have also demonstrated the significance of the results in systems evaluation through the effect on the thermal derivative, or "radiation contrast," used in evaluating infrared scanning systems such as the FLIR. The methodology, *per se*, is applicable only to isothermal clouds and isotropic scattering although these are not necessarily fundamental limitations on the method. In another preliminary study we have extended the method to include non-isothermal clouds and other practical effects using various approximations [13,14]. Other efforts are underway to evaluate the results against field measurements [16].

References

1. Sutherland, R.A., "Determination and use of IR Band Emissivities in a Multiple Scattering and Thermally Emitting Aerosol Medium," ARL-TR-2688, June 2002.
2. Hoock, D.W. and R.A. Sutherland, "A Combined Obscuration Model for Battlefield Induced Contaminants, COMBIC," ASL-TR-0213, 1984.
3. Kondratev, K. Ya, *Radiation in the Atmosphere*, Academic Press, NY & London, 1969.
4. Chandrasekhar, S., *Radiative Transfer*, Dover Publications, New York, 1960.
5. Van de Hulst, H.C., *Multiple Light Scattering tables, Formulas, and Applications, Vol 1*, Academic Press, 1983.
6. Sigel, R. and J.R. Howell, *Thermal Radiation Heat Transfer*, McGraw-Hill, New York, Chapter 20, 1972.
7. Abramowitz, M. and I. Stegun, "Handbook of Mathematical Functions," Dover Press, New York, NY, 1970.
8. Sutherland, R.A., 1982, "Field measurement requirements for electro-optical obscuration modeling," *Proceedings of the Society of Photo-Optical Instrumentation Engineers*, 356:14-20.
9. Wolfe, W. L., *Radiation Theory*, Ch. 1, Vol. 1, *The Infrared and Electro-Optical Systems Handbook*, SPIE Press, Bellingham, WA (USA), 1993.
10. Mermelstein, M.D., K.A. Snail, and R.G. Priest, "Spectral and radiometric calibration of midwave and longwave infrared cameras," *Opt. Eng.* 39(2) 347-352, 2000.
11. Jacobs, P.A., *Thermal Infrared Characterization of Ground Targets and Backgrounds*, SPIE Optical Engineering Press, Bellingham, WA (USA), 1996.
12. Holst, G.C., "Common Sense Approach to Thermal Imaging," published by SPIE—The International Society for Optical Engineering, Bellingham WA, 98227-0010, 2000.
13. Sutherland, R.A., J.C. Thompson, and S.D. Ayres, "Infrared Scene Modeling in Emissive, Absorptive, and Multiple Scattering Atmospheres," *Proceedings of SPIE*, April 2001.
14. Sutherland, R.A., J.C. Thompson, and J.D. Klett, "Effects of Multiple Scattering and Thermal Emission on Target-Background Signatures Sensed through Obscuring Atmospheres," *Proceedings of SPIE*, April 2000.
15. Kuhlman, et al., "Evaluation of Physical Properties of a Foreign Smoke," Contractor Report FMTR-1620-90030-001-94, National Ground Intelligence Center, August 1995.
16. Sutherland, R.A. and J.E. Butterfield, "PILOT-81 VVA Experiment," ARL Technical Report, in preparation, June 2002.

REPORT DOCUMENTATION PAGE			<i>Form Approved</i> OMB No. 0704-0188	
<p>Public reporting burden for this collection of information is estimated to average 1 hour per response, including the time for reviewing instructions, searching existing data sources, gathering and maintaining the data needed, and completing and reviewing the collection information. Send comments regarding this burden estimate or any other aspect of this collection of information, including suggestions for reducing the burden, to Department of Defense, Washington Headquarters Services, Directorate for Information Operations and Reports (0704-0188), 1215 Jefferson Davis Highway, Suite 1204, Arlington, VA 22202-4302. Respondents should be aware that notwithstanding any other provision of law, no person shall be subject to any penalty for failing to comply with a collection of information if it does not display a currently valid OMB control number.</p> <p>PLEASE DO NOT RETURN YOUR FORM TO THE ABOVE ADDRESS.</p>				
1. REPORT DATE (DD-MM-YYYY) July 2002		2. REPORT TYPE Final		3. DATES COVERED (From - To) August 1998–October 2001
4. TITLE AND SUBTITLE Verification of the Aerosol Emissivity Model, PILOT-EX			5a. CONTRACT NUMBER	
			5b. GRANT NUMBER	
			5c. PROGRAM ELEMENT NUMBER	
6. AUTHOR(S) Sutherland, Robert A.			5d. PROJECT NUMBER	
			5e. TASK NUMBER	
			5f. WORK UNIT NUMBER	
7. PERFORMING ORGANIZATION NAME(S) AND ADDRESS(ES) U.S. Army Research Laboratory Information & Electronic Protection Division Survivability Lethality Analysis Directorate (ATTN: AMSRL-SL-EM) White Sands Missile Range, NM 88002-5513			8. PERFORMING ORGANIZATION REPORT NUMBER ARL-TR-2689	
9. SPONSORING/MONITORING AGENCY NAME(S) AND ADDRESS(ES) U.S. Army Research Laboratory 2800 Powder Mill Road Adelphi, MD 20783-1145			10. SPONSOR/MONITOR'S ACRONYM(S)	
			11. SPONSOR/MONITOR'S REPORT NUMBER(S) ARL-TR-2689	
12. DISTRIBUTION/AVAILABILITY STATEMENT Approved for public release; distribution unlimited				
13. SUPPLEMENTARY NOTES				
14. ABSTRACT <p>We report on the verification of the multiple scattering and thermal emission model PILOT-EX described in a previous publication and extend the scope to include non-isothermal clouds. We also verify the expressions leading to the thermal version of the radiative transfer equation, fill in the details of the Gaussian spherical cloud formulation, describe methods for treating the emissivity correction for limited bandpass instruments, and discuss the significance of the results in terms of radiation contrast and aerosol-induced noise. We extend the model to include arbitrary "embedded sources" and verify results against standards in the literature over a variety of incident angles and demonstrate the significance of the results in computing infrared contrast for use in imaging systems performance analysis. A major finding is that comparisons with known (isothermal) solutions show agreement to within five significant figures for the case of plane layers for both normal incidence and various slant path angles. Also, preliminary results for the case of temperature stratification demonstrate a significant build up of radiance in the (hotter) cloud interior, which leads to lower values of the apparent emissivity for non-isothermal clouds.</p>				
15. SUBJECT TERMS emissivity, multiple scattering, thermal emission, atmospheric obscurants, aerosols, smoke, clouds, modeling, simulation				
16. SECURITY CLASSIFICATION OF:			17. LIMITATION OF ABSTRACT SAR	18. NUMBER OF PAGES 45
a. REPORT U	b. ABSTRACT U	c. THIS PAGE U		19a. NAME OF RESPONSIBLE PERSON R.A. SUTHERLAND
				19b. TELEPHONE NUMBER (Include area code) (505)678-4520